Unterschrift BetreuerIn

TECHNISCHE UNIVERSITÄT WIEN

DIPLOMARBEIT

Pulsed-laser growth of $La_{0.8}Sr_{0.2}MnO_3$ on $SrTiO_3(001)$

ausgeführt am Institut für Angewandte Physik
der Technischen Universität Wien

unter der Anleitung von
Univ.Prof. Dipl.-Ing. Dr.techn. Ulrike Diebold
Dr. Michele Riva
und
Erik Rheinfrank, MSc., BSc.

durch

Michael Brunthaler, BSc.
Matrikelnummer 01556037
[redacted]

Wien, 09.05.2022

Unterschrift StudentIn

Kurzfassung

Die Oberflächen von $La_{0.8}Sr_{0.2}MnO_3(001)$ (LSMO) sind hochkomplexe Systeme wegen der vielen Anordnungsmöglichkeiten der Oberflächenatome in Abhängigkeit von der Stöchiometrie. Mittels Laserstrahlverdampfens wurde eine Reihe von heteroepitaktischer Schichtwachstumsexperimente von LSMO auf $SrTiO_3(001)$ durchgeführt. Die Experimente sind motiviert durch jüngste Ergebnisse von $SrTiO_3$ auf $SrTiO_3(110)$ und LSMO auf $SrTiO_3(110)$, die das Verhalten von derartigen Oberflächen untersucht haben. Für die *ex-situ* Präparation des $SrTiO_3$ Substrats wurde ein detailliertes Protokoll erarbeitet, das für möglichst gleichmäßige Ausgangsbedingungen für die darauf folgenden Schichtwachstumsexperimente sorgt. Sowohl bei den dünnen (5.1 nm) LSMO Schichten als auch bei den $SrTiO_3$ Substraten wurden aufgrund von präferentieller Zerstäubung Erkenntnisse über die Oberflächenstöchiometrie gewonnen. Weiters wurde eine Reihe von Standardoberflächenphysiktechniken zur Charakterisierung der Oberflächen eingesetzt. Darunter fallen Röntgenphotoelektronenspektroskopie (XPS), Beugung niederenergetischer Elektronen an Oberflächen (LEED), Beugung hochenergetischer Elektronen bei Reflexion (RHEED), Rastertunnelmikroskopie (STM) und Rasterkraftmikroskopie (AFM). In Abhängigkeit von der vorherrschenden Stöchiometrie an der Oberfläche wurden zwei Oberflächenrekonstruktionen identifiziert. Die in unseren Experimenten am häufigsten vorkommende Rekonstruktion teilt Merkmale mit zweidimensionalen Quasikristallen. Die Details dieser Rekonstruktion wurden analysiert und ein Vorschlag für den Aufbau wird gezeigt.

Abstract

The surfaces of $La_{0.8}Sr_{0.2}MnO_3(001)$ (LSMO) are highly complex systems due to the many possibilities of atomic surface arrangements with varying stoichiometry. In this thesis, the preparation of thin films of LSMO on $SrTiO_3(001)$ substrates via pulsed laser deposition (PLD) is explored, following up on recent studies of similar studies of $SrTiO_3$ on $SrTiO_3(110)$ and LSMO on $SrTiO_3(110)$. A detailed protocol for an *ex-situ* cleaning procedure of the substrate is included. Preferential sputtering is explored, which gives insights into the surface stoichiometry of the films. Standard surface science techniques including X-ray photoelectron spectroscopy (XPS), low-energy electron diffraction (LEED), reflection high-energy electron diffraction (RHEED), scanning tunnelling microscopy (STM) and atomic force microscopy (AFM) are applied to characterize the surface. Two main surface reconstructions are found depending on the stoichiometry of the surface. The most prevalent surface reconstruction exhibits quasicrystal characteristics. A structure for the surface reconstruction is proposed.

Contents

1 Introduction

The following sections give a short overview and motivation for the thesis. The materials are introduced and the details of growth processes are reviewed. In thin film production by pulsed laser deposition (PLD), many growth parameters have to be considered in order to obtain the desired output. An overview for the role of the thermodynamic and kinetic processes in PLD thin-film growth will be given.

Chapter 2 outlines the principles of the methods in this thesis. It introduces how these methods are used to gain insights in the substrate quality before growth, the growth process itself and the characterization of the resulting thin films.

Chapter 3 focuses on the substrate used for the growth, $SrTiO_3(001)$, and its *ex-situ* and *in-situ* preparation. The details of the growth-process of $La_{0.8}Sr_{0.2}MnO_3(001)$ are discussed, and finally a characterization of the films is presented.

1.1 $La_{0.8}Sr_{0.2}MnO_3$ (LSMO)

Perovskite oxides are some of the most versatile materials with a wide range of physical and chemical properties. For instance, they can be metallic, semiconducting, superconducting, insulating, dielectric, piezoelectric, thermoelectric, pyroelectric or electrocaloric, depending on the crystal structure and doping of the system (for one example see Fig. 1.2). The ideal perovskite structure is cubic (see Fig. 1.1). In the unit cell of an ABO_3 perovskite, where A and B represent the two cations, the A cation sits in the center of the cube. The B cation sits on the corner of the unit cell and has an octahedral coordination to oxygen atoms, which are located in the middle of the cube's edges. The possible candidates for A and B sites can be

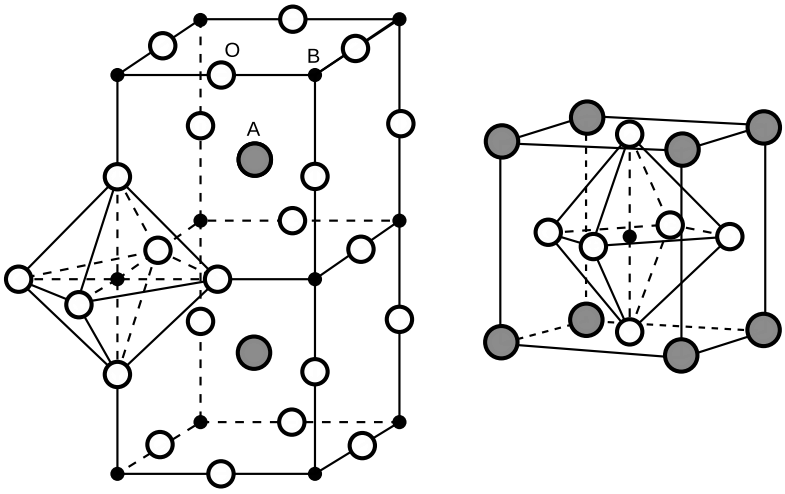

Figure 1.1: Cubic perovskite ABO_3 structure. In LSMO, A stands for La and Sr and B stands for Mn. Reprinted from [1].

from all over the periodic table, which makes perovskite oxides especially suited for chemical tailoring.

The many exceptional properties of these materials have already found their applications. But the mechanisms, especially in chemical reactions, are often still not well understood at the atomic scale. For more insights into the physical and chemical mechanisms and eventually optimizations in applications, knowledge about the surfaces and interfaces is needed.

To investigate the surfaces of perovskite oxides at the atomic scale, one needs well-defined systems such as single crystals. However, these are often not commercially available. Moreover, as it will be shown in this thesis, the growth of high-quality perovskite oxide films is challenging. For these reasons, the knowledge on the surfaces of perovskite oxides is limited, with some exceptions [1–3].

This thesis focuses on (0.5 wt.%) niobium doped $SrTiO_3$ and $La_{0.8}Sr_{0.2}MnO_3$ (LSMO), as substrates and thin films, respectively. $SrTiO_3$ has ideal cubic perovskite structure (unit cell length 3.905 Å) and is well suited as a substrate with a lattice mismatch of 0.74% compared to bulk LSMO.

$SrTiO_3$ is one of the best known perovskite oxides regarding surface structures. $SrTiO_3(001)$ shows a wide range of surface reconstructions, often characterized

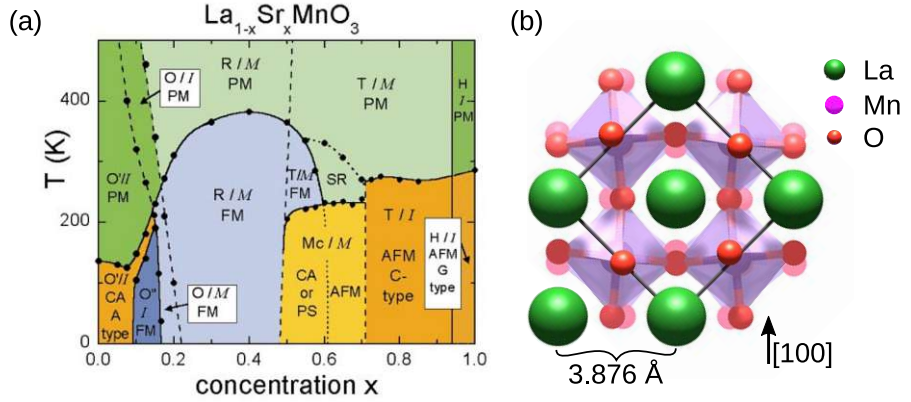

Figure 1.2: (a) Phase diagram of $La_{1-x}Sr_xMnO_3$ as a function of the Sr doping level. The crystal and magnetic structures are indicated [Jahn-Teller distorted orthorhombic: O', orthorhombic O', orbital-ordered orthorhombic: O", rhombohedral: R, tetragonal: T, monoclinic: Mc, hexagonal: H; paramagnetic: PM (green), short-range order: SR, canted: CA, A-type antiferromagnetic structure: AFM (yellow), ferromagnetic: FM (blue), phase separated: PS] (b) The rhombohedral structure of the perovskite $La_{0.8}Sr_{0.2}MnO_3(001)$. Notice the slightly tilted and rotated MnO_6 octahedra, which determine the $(\sqrt{2} \times \sqrt{2})$ unit cell in the (001) plane. Phase diagram in (a) reprinted with permission from [5]. Copyright 2002 by the American Physical Society. Rendering in (b) by Michele Riva.

by large unit cells [4]. The observed and partially solved surface reconstructions are representative for the inherent challenges one faces in the research of complex oxide surfaces. The surfaces are sometimes insulating, polar or can have mixed cation terminations. On this front, the observed experimental data exceeds the theoretical and computational state of the art. The complexity of these structures has been known for many years. Rules and general trends have been formulated for determining structural models of metal perovskite-oxide surface reconstructions (e.g. Pauling's rules applied to surfaces [4]).

LSMO can show a variety of different crystal structures depending on the doping level (see Fig. 1.2a). The LSMO films grown in this thesis have a Sr doping close to 20%. At this doping level, LSMO has a rhombohedral structure and shows Jahn-Teller distortion. The rhombohedral nature is depicted in Fig. 1.2b. The MnO_6 octahedra are tilted and rotated. The unit cell is enlarged to a $(\sqrt{2} \times \sqrt{2} \times 2)$ unit cell, but the structure can still be viewed as a pseudocubic structure with unit cell length of 3.876 Å.

LSMO has been researched for structural, magnetic, electronic properties among others [6–12]. Furthermore, in LSMO thin films, e.g. thickness-dependent ferromagnetism, metallicity [6] and metal-to-insulator transitions [8] have been reported. However, literature for the surface properties of LSMO single-crystalline thin films is scarce. One example from Kelley et al. [13] is LSMO(001) films on $NdGaO_3$(001) pseudocubic substrates. There, the authors identified a long-range surface reconstruction using LEED, and proposed a structural model. However, STM studies on LSMO(001) are needed to confirm or refute the proposed models. In this thesis, we observed the same long-range reconstruction of Kelley et al. and were able to image it in STM. Section 3.2 compares in detail our and the literature's findings.

As mentioned above, the prerequisite to performing systematic STM analysis is to possess atomically flat films. LSMO films of the needed quality have been previously achieved on the (110) orientation [2, 14]. Systematic studies of the growth parameters have shown that only a narrow window of substrate temperatures and oxygen partial pressures optimize thin-film growth. Small deviations from the optimal conditions lead to non-stoichiometric accumulations of clustered material, which is not desired. However, LSMO(110) surfaces can tolerate near-surface off-stoichiometries by forming many different surface reconstructions. Also different annealing cycles, with oxygen partial pressures of 0.2 mbar to reducing conditions in UHV, can change the reconstructions, again depending on the cation stoichiometry. Surfaces with smaller clusters can even be recovered by preferential sputtering or by additional deposition of A- or B-site cations. As shown in more detail in the next chapters, the growth of (001)-oriented LSMO films has some common traits with (110)-oriented ones.

1.1.1 Solid Oxide Fuel Cells (SOFCs)

This section aims to introduce the principle of solid oxide fuel cells (SOFCs) and motivate our research of the cathode material LSMO.

Fuel cells are electrochemical cells that can convert chemical energy into an

electrical current. The principle of a solid oxide fuel cell (SOFC) is seen in Fig. 1.3. A SOFC consists of an anode and a cathode, with an electrolyte in between. Via the chemical reactions occurring at the different interfaces, an electrical current can be produced between anode and cathode. Lanthanum manganites are one of the most common choices for cathodes because they are compatible with good electrolyte materials (e.g. yttria stabilized zirconia—YSZ).

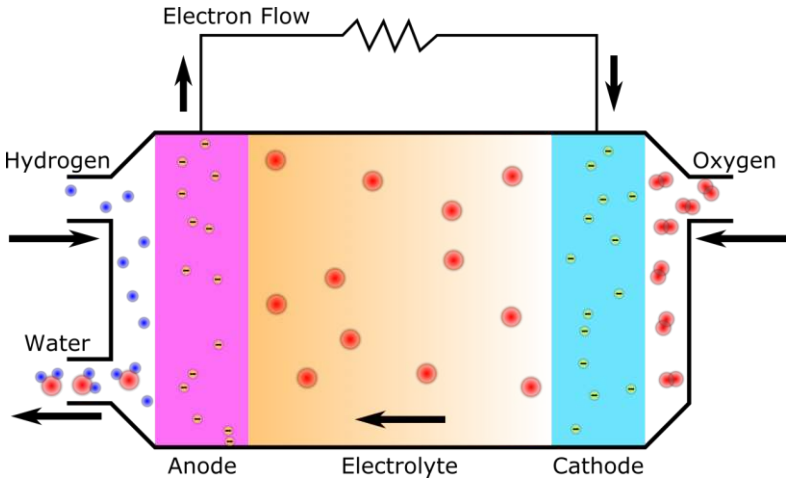

Figure 1.3: Schematic diagram demonstrating the general operating principles of a solide oxide fuel cell.

SOFCs typically operate in the range between 700°C to 1000°C. At these high temperatures the ceramics become electronically and ionically active. Because of the extreme requirements for the materials (e.g. conducting ions and current, chemical/thermal properties, long term stability), the optimization of the possible compounds is an active field of research.

A schematic overview of SOFCs is shown in Fig. 1.3. The anode side is electrochemically oxidized according to $2H_2 + 2O^{2-} \rightarrow 2H_2O + 4e^-$ for hydrogen fuel. To be well functioning it has to have, among other things, high electrical and ionic conductivity, high porosity for fuel supply, aversion for carbon deposition and chemical and thermal expansion compatibility with electrolyte and cathode. The most common material for hydrogen-fuel-based SOFCs is Ni/YSZ cermet.

In electrolytes, the oxygen-ion transport between the electrodes takes place. It

electronically separates the anode from the cathode while simultaneously allowing an exchange of conducting ions. Most high-temperature fuel cells operate by oxygen-ion conduction from the air electrode to the fuel electrode. Therefore, the electrode material has to have oxygen-ion vacancies and a low energy barrier for oxide ion migration between unoccupied anionic sites.

At the cathode/electrolyte interface, oxygen from air is converted to oxygen ions. The electrolyte transports them to the anode, where the reaction with, e.g., hydrogen takes place to produce water.

The oxygen-incorporation process at the cathode is one known limiting factor in the efficiency of SOFCs. Models describing it mainly factor in the availability of surface oxygen vacancies at the cathode, the availability of electrons, and the position of the oxygen $2p$ band center. Theoretical studies typically assume bulk-truncated surfaces to model the oxygen incorporation, although there exists research showing that the atomic-scale structure can have significant influence on the process [15]. A systematic approach addressing different crystallographic orientations and studying the influence of surface reconstructions is sought after to better understand the oxygen incorporation at the cathode's surface. Commercially available materials are often in powder form or have multiple crystallites in different directions, which makes it nearly impossible to resolve atomically. This thesis uses a controlled single crystal growth combined with standard surface science methods (chapter 2) to reduce the complexity of this matter.

1.2 Growth Processes

This section gives an overview for growth processes in PLD. A distinction between growth in a thermodynamically stable system and the influence of non-equilibrium kinetics far from equilibrium is made. The combination of thermodynamics and kinetics describes vapour-phase deposition techniques such as PLD that grow films not in thermodynamic equilibrium, and where kinetic effects play a major role.

1.2.1 Thermodynamic growth modes

Systems that are well described by thermodynamic growth modes are typically in, or close-to equilibrium. Nucleation is caused by local fluctuations from equilibrium that lead to a phase transition from gas to solid phase. Subsequent processes that depend on the free energies of film surface (γ_F), substrate surface (γ_S) and the interface (γ_I) between the two dictate the growth. Once the nuclei saturate the surface, crystallization takes over and, depending on the total surface energy, a film will grow in a certain mode.

For weak or no bonding between substrate and film, a wetting layer on the substrate increases the interface energy γ_I, therefore three-dimensional island growth is preferential (Fig. 1.4c), in what is called the Volmer–Weber regime. On the other hand, if the total surface energy of the saturated substrate ($\gamma_F + \gamma_I$) is lower than the surface energy of the pristine substrate γ_S, the growth proceeds in a layer-by-layer fashion, that is, one layer grows only after the layer below is complete (Fig. 1.4a). The reason for this growth mechanism is the strong bonding between film and substrate that lowers the free energy at the interface γ_I. If additional stresses on the film are introduced, e.g. via a lattice mismatch with the substrate, another mode can emerge from the layer-by-layer growth (Fig. 1.4b), called Stranski–Krastanov growth mode. In this case, the growth proceeds layer by layer until the stress caused by the lattice mismatch costs too much energy. With increasing film thickness the elastic energy builds up, which ultimately leads to the misfit dislocations and island growth on top of the initial film.

In heteroepitaxy, substrate and film lattice often do not match and therefore biaxial strain will lead to an elastic energy that grows with increasing layer thickness. This can lead to misfit dislocations that relieve the biaxial strain when the subsequent change in elastic energy becomes comparable to the increase in interfacial energy.

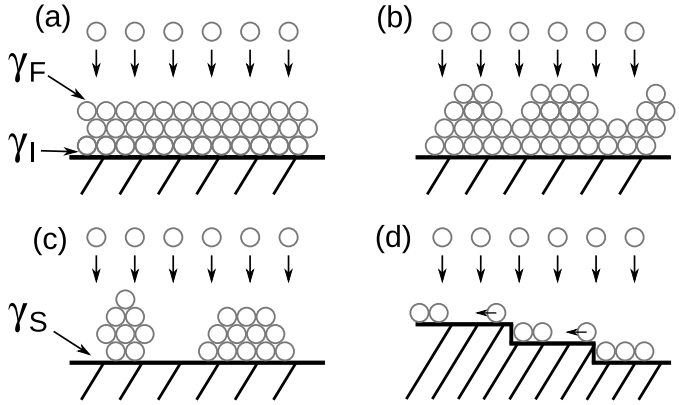

Figure 1.4: Film growth modes: (a) layer-by-layer (Frank–Van-der-Merwe); (b) island (Stranski–Krastanov); (c) island (Volmer–Weber); (d) step flow. Adapted from [16].

1.2.2 Growth kinetics

As already mentioned above, film growth by PLD is not in thermodynamic equilibrium. Unlike in the thermodynamic regime, in the kinetic regime the atomic details and interactions of the surface and the adsorbate come into play. Therefore, kinetic limitations associated with finite rates of mass transport processes can influence the actual growth mode. Especially, the diffusion of atoms on a flat terrace and across a step edge, namely *intralayer* and *interlayer* mass transport, have to be taken into account.

In homoepitaxy, the growth behaviour is determined by the surface diffusion coefficient D_S of the adatoms, the sticking probability (at steps) P_S and the energy barrier ΔE_{ES} to step down a terrace. D_S is generally written as

$$D_S = \nu a^2 \exp\left(-\frac{E_{\text{diff}}}{k_B T}\right) \tag{1.1}$$

with ν as the attempt frequency, a the characteristic jump distance and E_{diff} the diffusion activation energy. Equation 1.1 illustrates the importance of temperature for diffusion. Low temperatures inhibit movement on the surface, while high temperatures facilitate it. For the above-mentioned *interlayer* mass transport, one can consider the shape of the potential energy curve for an adatom near a step (Fig. 1.5). An adatom approaching the step from the lower side would stay at the

step because of the increased coordination and therefore higher binding energy. For this reason, diffusion up the step is normally neglected.

The coordination of the adatom crossing the step from the upper side is reduced when it moves down, which can act like an barrier. This additional energy barrier is known as the *Ehrlich–Schwoebel barrier* ΔE_{ES} and it modifies the diffusive step-edge transmission of adatoms.

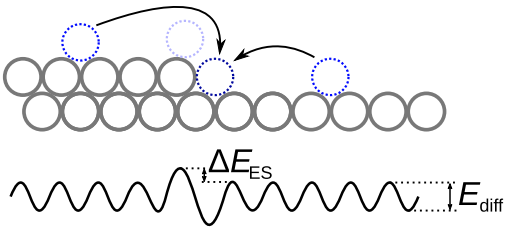

Figure 1.5: Schematic representation of the potential energy variations associated with a monoatomic step. ΔE_{ES} represents the Ehrlich–Schwoebel barrier, which an adatom has to overcome (adatom left to right) in addition to the terrace-diffusion barrier E_{diff} in order to move down the step edge. Adapted from [17].

Taking the adatom intralayer mobility into account, the growth modes are *step-flow* growth (Fig. 1.4d), *layer-by-layer* growth and *multilayer* growth. Step-flow growth emerges close to equilibrium at high intralayer mobility and therefore the adatoms reach a step before nucleating on a terrace. In layer-by-layer and multilayer growth, which look similar to Fig. 1.4a and Fig. 1.4c respectively, the terrace width is greater than the adatom migration length and the nucleated atoms form their own steps. Depending on the Ehrlich–Schwoebel barrier, additional adatoms will either participate in completing a full layer first (large interlayer mass transport) or start multilayer 3D growth (small interlayer mass transport).

2 Methods

In this chapter, the experimental methods are described. Many of the applied techniques are commonly used in experimental surface physics, therefore the description is kept short. Greater focus is put on the pulsed laser deposition (PLD) system, since its parameters and technical aspects influence the experiments carried out in this thesis most notably. It should be empathized that the experimental setup is rather uncommon, since it combines the PLD growing method with the analysis capabilities of ultra high vacuum (UHV) surface science techniques (e.g. LEED, XPS, STM). This combination facilitates reproducibility and accuracy and limits the possible source of errors due to different starting points or contaminations.

2.1 Pulsed Laser Deposition (PLD)

Pulsed laser deposition is a widely used method for evaporative film growth. The general idea is relatively simple. A ultraviolet (UV) laser emits a short pulse (10–50 ns) that is focused onto the desired target inside a vacuum system. The laser ablates material at the target, which will be deposited onto a substrate via a plasma plume. High oxygen partial pressure is used to sustain the plasma plume and the substrate is additionally heated by an infrared (IR) laser (or more commonly by a filament-based heater) to facilitate the diffusion of the deposited species on the substrate's surface. This allows for very precise growth control, because every pulse typically deposits submonolayer amounts.

Physical mechanism

A complete description of the physical processes in PLD combines many mechanisms, e.g. coupling of electromagnetic radiation with condensed matter, initial production of the plasma, the expansion away from the target, and the condensation on the substrate. One important aspect is the mechanism involved the light–material interaction when ablating from the target. The energy transfer is dominated by photoionisation and inverse Bremsstrahlung. The laser pulse is absorbed in the surface region of the target. The electromagnetic energy is at first converted into electronic excitations, which produces a dense layer of vapour in front of the target. Due to the high energy imposed onto a small area on the target, the material cannot dissipate the induced heat. When the pulse is fully absorbed, the pressure and temperature rise rapidly, causing ionization. The subsequent expansion of this layer is called the plasma plume, during which the thermal and ionization energies are converted into kinetic energy of the ablated target atoms. The kinetic energy is lowered by many collisions during the expansion in background gas (typically 10^{-3}–1.0 mbar oxygen for deposition of oxides). In Fig. 2.1, a long-exposure photograph of multiple plasma plumes can be seen.

The characteristic time lengths for the laser-pulse–deposition process and mean diffusion time are far apart for most deposition parameters—microseconds and milliseconds respectively. Therefore, PLD growth is considered far from thermodynamic equilibrium, since the deposition process can be viewed as near instantaneous for each pulse, followed by an comparatively long annealing phase in between. Depending on the pulse frequency, the growth rate can be varied independently, which is a unique feature in thin film growth techniques.

PLD parameters

Although the principle of PLD is rather straightforward, many challenges have to be addressed to produce films of single-crystalline quality. Indeed the growth process strongly depends on several parameters, especially for complex multicomponent systems. The parameters of the background pressure, laser fluence

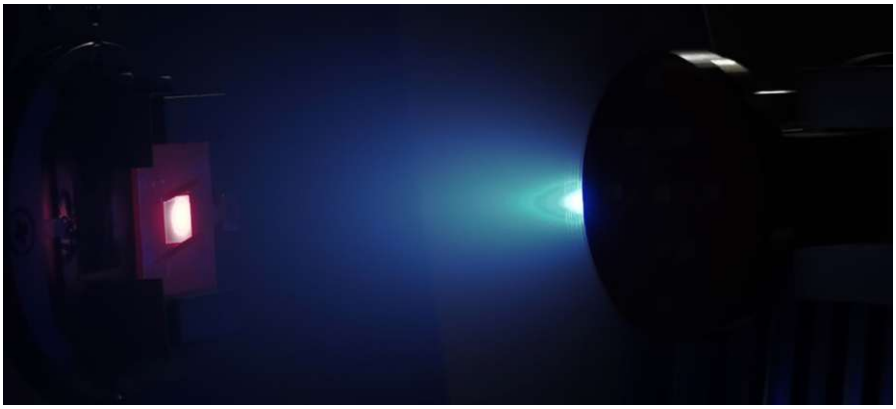

Figure 2.1: Long exposure photograph of multiple plasma plumes (right) ejected from the LSMO target onto an $SrTiO_3$ sample (left) heated to a temperature of 800°C.

and target–substrate distance dictate the kinetic energy and stoichiometry of the material hitting the surface. As a consequence, they will influence many of the films' properties, including their composition, their crystal structure, and their surface morphology.

The oxygen partial pressure is divided in three regimes that relate to the mean free path of the ablated material. Very low pressures result in a long mean-free path, which exceeds the target–substrate distance. On the other hand, very high pressures lead to the so-called shock-wave regime, in which all species slow down at the same rate and are more restricted in movement. For an intermediate range of oxygen partial pressure, the resulting film composition is influenced by preferential scattering depending on the species. For higher pressures in this intermediate regime, the film will enrich with heavier species.

Additionally, laser pulse duration, beam divergence, pulse energy and energy density, pulse-to-pulse standard error, absorption at the target surface, and repetition rate must be controlled precisely to ensure the reproducibility of the results from chamber to chamber.

On the receiving side of the plasma, it is important to have a clean and well defined surface. Substrate cleaning will be described in detail in Section 3.1. Moreover, the substrate temperature also plays a crucial role. Firstly, high temperatures equate to high diffusion of the landing species and a high chance for

finding their energetically favourable configuration. The oxygen partial pressure p_{O_2} and substrate (growth) temperature T also relate to the oxygen chemical potential, which can strongly affect the diffusion of cations. The oxygen chemical potential $\mu_{O_2}(T, p_{O_2})$ can be written as

$$\mu_{O_2}(T, p_{O_2}) \propto k_B T \ln\left(\frac{p_{O_2}}{p_0}\right) \tag{2.1}$$

where k_B is the Boltzmann's constant, $p_0 = 1$ bar, and T is the absolute temperature in Kelvin. It has been reported that a change in oxygen chemical potential during sample preparation can enhance surface diffusion, and produce flatter morphologies [18].

Setup

Figure 2.2 shows a schematic representation of the PLD system that was used within this thesis, which is equipped with high-pressure reflection high-energy electron diffraction (RHEED), an IR-heating laser and an UV laser. The UV laser with a wavelength of 248 nm (KrF excimer laser) is used for ablating the target. The laser travels through a set of optical mirrors and a focusing lens *ex-situ* before entering the UHV system. The laser energy can be adjusted with an attenuator and is measured outside the PLD chamber via an exit window (not shown). The IR laser keeps the sample at the desired temperature. As depicted in Fig. 2.2, the laser hits the sample directly on the backside via a hole in the sample plate. During the growth process, RHEED can be used to monitor the growth in real time, as detailed later below. A combination of continued oxygen flow with adjusted pumping guarantees a stable oxygen background pressure.

Ablation targets

While there is good commercial availability for targets used in PLD, custom stoichiometry or materials can be a challenge to synthesize. The ablation targets should have a high optical absorption coefficient at the used laser wavelength,

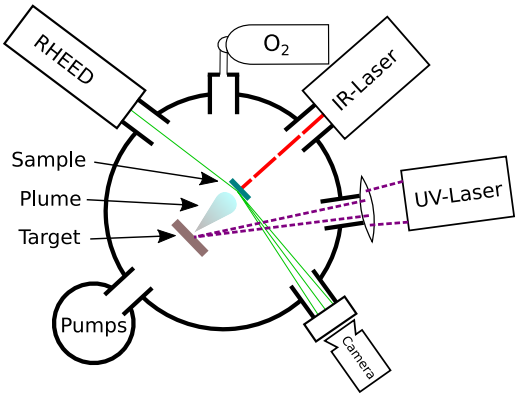

Figure 2.2: Schematic view of the PLD setup. The desired material can be ablated from the target via an UV-Laser. At the same time, the sample can be heated by an IR-Laser and the growth can be controlled in real time by measuring intensity curves of the diffracted RHEED beam.

while simultaneously meeting the standards for density, homogeneity, composition and purity. A too low density and insufficient homogeneity can lead to the removal of big clusters during ablation. This is not desired in epitaxial growth, since it would introduce a local imbalance in the crystallization process. The composition of the target does not matter as much as the density, because the stoichiometry can also be tuned by the other PLD parameters. For a defect-free surface, the purity is quite important, as unwanted species can influence the geometric and electronic properties. Single crystals are well suited as target materials. But since thin film single crystal production is often the goal of this technique, the desired materials are often hard to obtain in single crystal form. Alternatively, sintered pellets are used. The used LSMO target is a sintered pellet. It has 94.1% of the ideal single crystal density and a purity of 99.996%, and was manufactured and characterized by Giada Franceschi [15].

The ablation target has to be treated with utmost care. Before the growth is started, the target is preablated to remove unwanted contamination. The target surface is ground regularly between growth experiments to avoid any unwanted changes in stoichiometry or roughness. To avoid dissolution, the *ex-situ* cleaning was done by sonication in water-free *n*-Octane and dried in air for 1 h at 150°C.

2.2 Scanning Tunnelling Microscopy (STM)

The STM is sometimes considered as the main innovation contributing the birth of nanotechnology, as it has enabled individual atoms and molecules to be imaged, probed and handled very precisely. A very sharp metal tip (ideally terminated by a single atom) is brought close to the sample to a distance in the nanometer range. The operation requires extremely fine movements of the tip relative to the sample, which are realized through piezoelectric ceramic actuators. If a bias voltage V is applied between the two electrodes (tip and sample), a current I_t flows between them even though they are not in contact. This is possible because of the quantum-mechanical process of electron tunnelling, in which an electron is described by delocalized wave functions. One can show that solving the stationary one-particle Schrödinger equations of unperturbed sample and tip, then using the Fermi golden rule while making several approximations, leads to the analytically manageable expression for the tunnelling current I_t:

$$I_\mathrm{t} = \frac{4\pi e}{\hbar} \int_{-\infty}^{\infty} \rho_\mathrm{tip}\left(E_\mathrm{F,tip} - eV + \epsilon\right) \rho_\mathrm{sample}\left(E_\mathrm{F,sample} + \epsilon\right) e^{-2\kappa s} \mathrm{d}\epsilon \tag{2.2}$$

where ρ is the density of states, E_F is the Fermi energy, 2κ is the inverse decay length and s is the tip-sample separation. The tunnelling current depends on the convolution of the density of states of tip and sample. Therefore, if the tip and sample geometries are not exactly known, it is hard to distinguish topographic effects from electronic effects.

STM images are generated by recording the tunnelling current as a function of the tip position while it is scanned across the sample surface. This can be done in two different operating modes, namely the *constant-height* and *constant-current mode*.

The *constant-height mode* fixes the height z of the piezo scanner while the tip is moved over the substrate at a constant bias voltage and the current between tip and sample is recorded. Features that protrude more over the surface correspond to a smaller tip-sample distance and lead to a larger tunneling current. The resulting

greyscale image of the tunnelling current can be viewed as the topography of the surface, although one has to consider that electronic effects cannot be entirely disentangled from topographic effects.

The *constant-current mode* mode makes use of a feedback control system, which allows the tip to maintain constant current, while the recorded z values produce the gray-scale image. Figure 2.3 (orange line) shows the path of the tip in the density of states landscape of a surface. This mode is used more frequently because it can be employed for any type of surface topography [19].

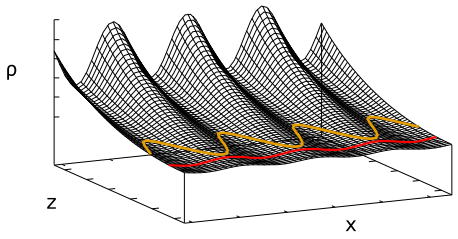

Figure 2.3: Representation of the different operating modes of a STM. The contour of constant density of states ρ is visualized in the constant-current mode as a orange line and the constant-height mode (red line) can be recognized as the variation of the density of states along a constant distance z from the surface. Figure adapted from [19].

The STM data collected in this thesis was used to determine surface structures of $SrTiO_3$(001) and LSMO(001). All images were taken in *constant-current mode* with positive sample bias voltage (which images empty sample states).

Tip treatment

The STM which was used in this work is equipped with a tungsten tip without the possibility of exchanging it without venting the system. For maintaining a well defined and sharp tip even over long periods without breaking vacuum, two techniques were used: tip sputtering with noble gas ions (Ar^+) and pulsing the tip with an elevated voltage for a short duration.

For the sputtering procedure, a shielding plate was used, which has a hole in the middle where the tip can be led through. This shielding plate is used as a safety precaution for reducing the sputtering damage on the piezo elements. The

measured ion current was in the microampere regime and typically fell steadily (e.g. from 2.5 µA to 1.1 µA). The duration was determined by historical evidence in the laboratory (e.g. 20 min), at an argon partial pressure of 5×10^{-6} mbar and at a voltage of 3 kV.

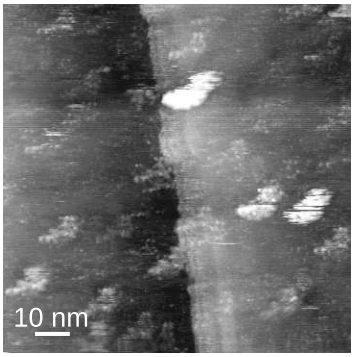

Figure 2.4: Example of a STM image of $SrTiO_3(001)$ with multiple tips. A step edge can be seen in the middle of the image. Because of the bad tip shape, a bright unknown feature is visible repeatedly; $U = 2.0$ V, $I = 0.1$ nA, 100×100 nm^2.

By applying a negative bias to the tip, field emitted electrons are focused and accelerated toward the sample by the strong field between the tip and the surface. This can also lead to a cleaner tip, because unwanted molecules and atoms on the tip may be emitted through field emission [20]. Typical voltages for pulses are up to -10 V. As an example of a badly shaped tip consisting of multiple contributing tips, an STM image of $SrTiO_3(001)$ can be seen in Fig. 2.4. The contribution to this data set by at least 10 tips can be identified, since the characteristic shape of a bright feature has been repeated multiple times in varying apparent height. It should be noted that the data has been taken in constant-current mode and at some of the x/y positions of the multi-tipped sensor, more than one of the tips provide tunnelling current contributions from different positions of the sample. This leads to the conclusion that a stronger 'main tip' likely recorded the bright feature and the surface atoms. The additional tips, elevated a few ångström, contribute in the form of 'shadow islands'.

Sample mounting

The sample plates have to firmly hold a sample while simultaneously not contaminating it (e.g. with glue). Moreover, to improve the sample temperature uniformity, the sample plates have a hole for direct heating of the substrate by an IR laser during growth. Nicrofer®, an alloy consisting mainly of nickel, chromium and iron, is stable at the high temperatures and oxygen pressures used within this thesis (1000°C, 0.2 mbar). The only drawback of Nicrofer® is its decline in the springiness of the clips (Fig. 2.5) upon repeated annealing cycles, which causes a weaker clamping of the sample to the plate, and may introduce unwanted vibrations during STM imaging.

The Nicrofer® clips are cut from 0.17 mm-thick foil with an approximate width of 0.7 mm. The spacer (arrow in Fig. 2.5) is made from three Nicrofer® stripes spot-welded together and spot-welded to the middle of the clip. The spacer is cut and filed to remove sharp edges. The clip is bent into clip-shape by a mold (not shown). Sample plates and clips are boiled in 20% HNO_3 and subsequently thoroughly rinsed in ultrapure water. Afterwards, the sample can be mounted as shown in Fig. 2.5. This leaves roughly 4×5 mm^2 of the 5×5 mm^2 sample surface free for film growth.

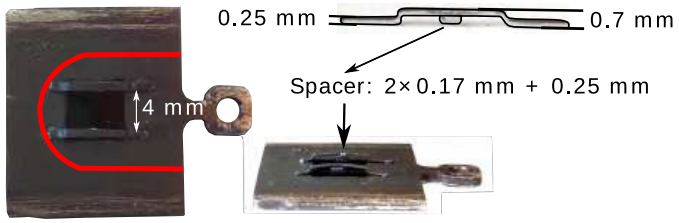

Figure 2.5: Sample mounting technique used within this thesis. The red line on the sample plate traces the limiting STM support. Figure adapted from [15].

Unfortunately, due to the increased stress on the sample mediated by the spacer, this technique often leads to cracking of samples during the initial annealing cycle. However, surviving samples show high resilience against many annealing cycles.

2.3 Low-Energy Electron Diffraction (LEED)

Theoretical considerations

A standard technique for many surface science laboratories is low-energy electron diffraction (LEED). It has been essential for detailed insights into surface structures since the 1960s. A schematic is shown in Fig. 2.6.

Due to the wave properties of the electrons, interference is possible and leads to diffraction patterns. A wavelength λ_e can be assigned to an electron, as postulated by de Broglie (Eq. 2.3):

$$\lambda_e = \frac{h}{p} = \frac{h}{\sqrt{2m_e E}} \tag{2.3}$$

Here, h is the Planck's constant, p is the momentum, m_e is the electron mass and E is the energy of the electron. In the range of electron energies typical of LEED, the de Broglie wavelength is of the same magnitude as the interatomic distances, which enables wave-like behaviour.

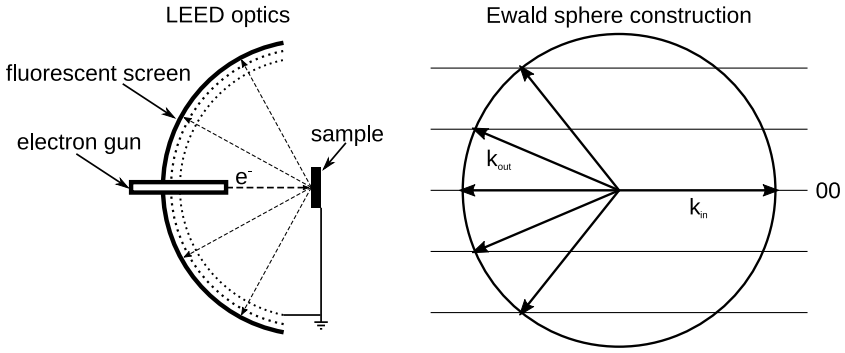

Figure 2.6: Schematic figure of a LEED setup (with a semi-circular screen) and the Ewald construction, which shows the possible scattering vectors $\vec{k}_{\text{out}}$. Adapted from [21].

Due to the small inelastic mean free path of the low-energy electrons injected into the sample the information reaching the screen (i.e., elastic electrons) only comes from the near surface layers. The recorded patterns of the reciprocal lattice facilitate decoding the surface reconstructions and lattice constants in real space [22].

Diffraction is based on interference of a monochromatic wave via scattering on a

(usually) periodic atomic lattice and the respective electrons. The Laue condition

$$\left(\vec{k} - \vec{k'}\right) \cdot \vec{a}_i = \Delta\vec{k} \cdot \vec{a}_i = 2\pi n_i \,, \quad n_i \text{ integer} \tag{2.4}$$

relates incoming waves to outgoing waves in elastic scattering. Here, $\vec{k}$ and $\vec{k'}$ are the wave vectors of the incoming and outgoing waves and $\vec{a}_i$ are the lattice unit vectors. For constructive interference $\Delta\vec{k}$ can be identified as a reciprocal lattice vector.

Every lattice vector $\vec{a_i}$ can be obtained from its reciprocal counter parts $\vec{a_i^*}$ (Eq. 2.5) and vice versa, with V being the volume for the real space unit cell.

$$\vec{a_i^*} = 2\pi \frac{\vec{a}_j \times \vec{a}_k}{V} \tag{2.5}$$

This information alone is often not enough to calculate the atomic arrangement or rearrangement on the surface, because the information contained in the phase can not be measured. For solving a surface reconstruction, a combination of multiple experimental methods and density functional theory simulations is common practice.

Experimental setup

The main components of a LEED setup are: An electron gun in with energies of 20 eV ranging up to 1000 eV, concentric retarding grids and a flat or semi-circular florescent screen to show diffraction maxima of the scattered electrons. The electron beam hitting the sample typically has a diameter of about 0.5–1.0 mm. The inelastically scattered electrons are filtered out via a suppressor grid held slightly below the electron beam energy. The remaining elastically scattered electrons are then re-accelerated with a screen voltage of (1-6) keV. Finally, a phosphorescent screen shows the diffracted electron beams via photoluminescence. If multiple surface reconstructions coexist on the surface, they will all be visible in LEED (see Section 3.1.2).

The LEED measurements in this thesis were taken in the energy range between

80 eV and 125 eV. The beam diameter in our system is about 0.7 mm. Furthermore, the electron signal at is increased by a micro-channel plate. The patterns are imaged using a camera with adjustable exposure time and noise reduction by averaging over multiple (e.g. 20) images. Usually multiple images are taken at different beam energies. Additionally, a dark-field image is taken at the same sample spot, without applying the screen voltage. Finally, a "flat" image is taken on the polycrystalline sample plate, which produces an image of uniform intensity without diffraction spots. In graphical post-processing with the software ImageJ [23], the three images are combined to produce a background-corrected image. Where necessary, a non-linear undistortion tool was used to rectify the pincushion distortion that deviates from the projection of the Ewald-sphere onto the flat LEED screen.

2.4 Reflection High-Energy Electron Diffraction (RHEED)

Reflection high-energy electron diffraction (RHEED) is the closely related to LEED and is a second important electron diffraction technique used in surface science [24]. The electrons are, as the name suggests, of higher energies (10–100 keV) and the electron beam is almost parallel to the sample. The grazing incident angle (3°–5°) leads to a similar surface sensitivity as in LEED. The fluorescent screen setup differs from LEED because of the changed geometrics (see Fig. 2.7a), although conceptually they are very similar. The screen is usually planar and the energy filtering of inelastic and secondary electrons can be neglected. The reason is the high intensities of the diffracted beams compared to the background. Because of its setup, where the electron source and screen are located around ≈ 50 cm away from the sample (see Fig. 2.2), it can be conveniently used together with other techniques.

The pattern of the recorded image can be explained via the Ewald sphere. The diffracted beam corresponds to the reciprocal lattice rods cut at a grazing angle (Fig. 2.7b). The diffraction spots shown in Fig. 2.7c are not very sharp, which is

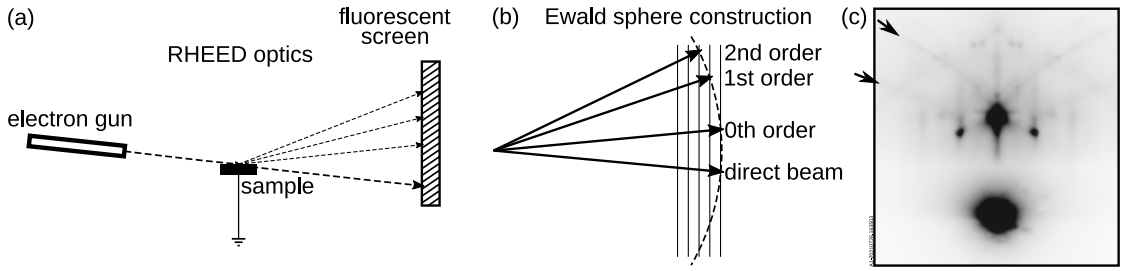

Figure 2.7: (a) Schematic representation of a RHEED setup (with a planar screen) and (b) the Ewald construction, which shows possible scattering vectors. (c) The $SrTiO_3(001)$-$(\sqrt{13} \times \sqrt{13}R33.7°$ surface is shown, where the direct beam and zeroth order beam can be identified. The so called 'Kikuchi' lines are also visible (e.g. from top left to the center of the image marked by black arrow). Adapted from [24].

due to the energy spread, angular spread, and defects in the surface. The image generally also does not only consist of diffraction spots, but also streaks and lines.

The lines visible in Fig. 2.7c, marked by black arrows, are called Kikuchi lines and occur due to non-linear multi-scattering effects. The electron diffraction of diffuse scattered electrons appear because of the high energies of the electrons. Clear and sharp Kikuchi lines indicate good bulk ordering.

RHEED can not only be used to investigate diffraction patters, but also to monitor growth processes in real time by monitoring the change in intensity of the RHEED specular spot. The specular spot intensity will vary as the growth proceeds. For ideal layer-by-layer growth, oscillations will be seen with maxima at fully completed layers. In step-flow growth, the intensity drops suddenly when material is deposited but soon recovers to the original intensity. The lowering of the intensity is because adatom deposition causes disorder at the surface. The intensity recovers because of the diffusion of the adatoms to the step edges, which restores the surface order.

Before growth, the intensity of the specular spot is maximised by adjusting the tilt and and azimuth angle of the substrate with respect to the incident RHEED beam. The result is in-phase diffraction from neighbouring terraces and makes the intensity sensitive to the step density within the coherence length of the electron beam. For multi-layer growth, the intensity decreases at first similar to layer-by-layer growth, but does not recover since the surface morphology changes sig-

nificantly from the initial state. Also combinations of these growth modes can be seen, e.g. oscillations combined with a steady intensity decrease will likely be layer-by-layer growth with subsequent appearance of islands.

In this thesis, RHEED provided real-time supervision of the thin-film growth of LSMO(001) on $SrTiO_3$(001). Sub-monolayer precision was achieved due to the combination of PLD and RHEED. The oscillations gave insights into the exact thickness of the grown films. Furthermore, the post-growth RHEED image (similar to Fig. 2.7c) provided information about the flatness of the films.

2.5 X-Ray Photoelectron Spectroscopy (XPS)

X-ray photoelectron spectroscopy (XPS) is a widely used method for investigating the chemical composition of surfaces. It makes use of the photoelectric effect, which is the emission of so-called photoelectrons from a material exposed to electromagnetic radiation. The surface sensitivity is determined by the distance that the photoelectrons can travel through the material without losing kinetic energy. Because this length, the inelastic mean free path, is in the nanometer range, most of the contribution to the recorded spectra originates from photoelectrons close to the surface [25]. The kinetic energy of the electron emitted through the XPS process can be described by Eq. 2.6

$$\epsilon_{\text{kin}}^{\text{sample}} = h\nu - \epsilon_{\text{B}} - \Phi_{\text{sample}} \tag{2.6}$$

$$\epsilon_{\text{kin}}^{\text{measured}} + \Phi_{\text{analyzer}} = \epsilon_{\text{kin}}^{\text{sample}} + \Phi_{\text{sample}} \tag{2.7}$$

where $\epsilon_{\text{kin}}^{\text{sample}}$ is the kinetic energy of the emitted electrons, $h\nu$ is the photon energy, ϵ_{B} is the binding energy, and Φ_{sample} is the work function of the surface. The measured kinetic energy of the photoelectrons at the detector is, by combination of Eq. 2.6 and Eq. 2.7, only dependent on the work function Φ_{analyzer} of the analyzer. This constant shift has to be known and typically lies in the range of 4–5 eV. From the recorded spectra, one can obtain information from the positions, intensities and

the width or shape of the peaks. In core-level emission, the rough peak positions correspond to the elemental composition of the sample surface, while the exact positions are characteristic of the chemical environment of the atoms [26].

The intensities are determined by the atomic concentrations, photon flux, transmission to the spectrometer and also the photoelectric cross section. Furthermore, the line shape can be Lorentzian or Gaussian or a mixture of both depending on the material, and the width corresponds to the lifetime of the photohole. For metals, a characteristic asymmetry can be observed, with elevated intensities on the lower kinetic energy side because of the excitation of a sea of electron–hole pairs across the Fermi level while the photoelectron is emitted [27]. Another contribution to a typical XPS spectrum comes from Auger electrons, which are produced in secondary processes in which the photohole is filled by an electron from a lower-binding-energy state. This releases a virtual photon which then transfers the energy to a second electron that is emitted into the vacuum. Auger electrons show at characteristic kinetic energies that depend on the involved energy levels and are thus independent of the exciting photon energy [28].

The measurements in this thesis were made using an Al Kα source, which radiates photons with an energy of 1486.6 eV. The photoelectrons produced from the sample were measured in a hemispherical analyser that allows tuning the specific passing kinetic energies to the detector.

2.6 *Ex-situ* Atomic Force Microscope (AFM)

The best-known descendant of the STM is likely the atomic force microscope (AFM) [29]. A basic sketch of an AFM setup is shown in Fig. 2.8. A sharp tip on a cantilever is placed very closely to the surface of a sample. The atomic forces act on the tip on the spring-like cantilever. A laser reflects from the cantilever onto a position-sensitive photodiode. The force acting on the tip is attractive at small distances (1–10 nm) from the surface because Van-der-Waals forces are present. For smaller distances, the atomic orbitals start overlapping and it results

in a repulsive force due to the Pauli exclusion principle.

The typical operating modes are called 'contact mode' and 'tapping mode'. In 'contact mode', the tip is dragged across the surface, and the cantilever bends depending on the surface morphology. With a feedback loop, the signal from the photodiode is processed to change the sample–tip distance accordingly to keep the deflection constant. The images presented in this thesis were acquired in air, and exclusively using the 'tapping mode'. In this mode, the tip is not scanned across the sample surface while in constant contact. Instead, the cantilever is vibrated close to its resonance frequency causing the tip to oscillate. The interaction with the surface is measured by the change of the oscillation amplitude. This mode mitigates damage to the surface as a result of contact with the tip.

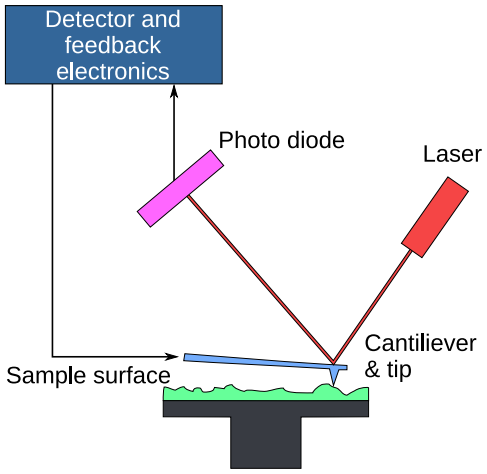

Figure 2.8: Basic sketch of the AFM setup used within this thesis. The laser is reflected onto a position-sensitive photodiode to measure the deflection of the cantilever. Reprinted from [30].

In the presented thesis, AFM was made use of for ensuring that $SrTiO_3(001)$ samples were as clean and flat as possible prior to transferring them to UHV, and to investigate the surface morphology of some LSMO(001) films.

3 Results

3.1 Substrate: $SrTiO_3(001)$

Single-crystalline (001)-oriented $SrTiO_3$ (0.5 wt.% Nb_2O_5) substrates from CrysTec GmbH were used for all experiments. The dimensions were $5 \times 5 \times 0.5$ mm^3 with a miscut of less than 0.2°. As mentioned in the introduction, $SrTiO_3$ has a perovskite structure, which has a cubic unit cell with the lattice constant of $a = 3.905$ Å. Along the (001) orientation, SrO and TiO_2 planes alternate. Due to the slight miscut of the surface, $SrTiO_3(001)$ exhibits terraces (the larger the miscut, the smaller the terraces). Terraces terminated by SrO or TiO_2 alternate on the surface. However, because different terminations are usually characterized by different sticking coefficient during growth, it is desirable to have surfaces exhibiting only one type of termination. During this thesis, the samples were treated *ex-situ* to exhibit only TiO_2-terminated terraces, as discussed below.

3.1.1 *Ex-situ* preparation

The recipe used for cleaning was adapted from previous works [15, 31]. Round-bottom flasks are used as a container for the substrates in the following steps, after cleaning them by boiling in 20% HNO_3 and rinsing them thoroughly with ultrapure water.

- Warming up the substrate in the sonicator for ≈20 min with each solvent (Ethanol/Isopropanol/3% Extran/ultrapure water). This step reduces unnecessary damage to the substrate due to abrasion on the corners (see Fig. 3.1a).

Then sonicating in the solvent once or twice for 20 min to remove surface contaminations as well as residues from mechanical polishing in the production process (see Fig. 3.1b$_1$).

- Rinsing multiple times with ultrapure water to remove the solvent and the contaminants. After short sonication with ultrapure water for 5 min, AFM images are taken as a quality assurance test (Fig. 3.1b$_2$). The steps are rough due to the polishing process of the manufacturer, but the terraces are visible. If contaminants persist, sonication with 3% Extran and ultrapure water is continued.

- Annealing in air at 1000°C for 3–12 h depending on the sample. After 3 h, some of the $SrTiO_3$ substrates still show somewhat jagged steps and sometimes screw dislocations. Additionally lines of contaminants appear in some samples (see black arrows in Fig. 3.1c). Steps become more straight upon annealing for a total time of 12 h. The lines seen in Fig. 3.1c are assigned to surplus SrO that reacts with CO_2 and H_2O at room temperature [32].

- Boiling the sample in ultrapure water for ≈5 min to remove the excess SrO compounds and other water-soluble contaminations (Fig. 3.1d). After blowing the sample dry with a non-reactive compressed gas (e.g. Ar, CO_2) it can be mounted for ultra-high vacuum (see mounting strategy in Section 2.2).

The reason why the ultrapure-deionized-water boiling is effective in removing excess SrO compounds lies in its ionic-bonding nature. With a few exceptions, ionic compounds are water-soluble materials. This approach has been shown to produce TiO_2-terminated surfaces [31, 33, 34]. In combination with the ≈ 0.4 nm high steps in the AFM line profile in Fig. 3.1e, a singly-terminated surface is safe to assume. If both terminations were present on the surface, one would see a measured apparent step height of ≈ 0.2 nm. Whether it is SrO or TiO_2 terminated is not completely clear, but TiO_2 termination is more likely due to the ultrapure deionised water treatment.

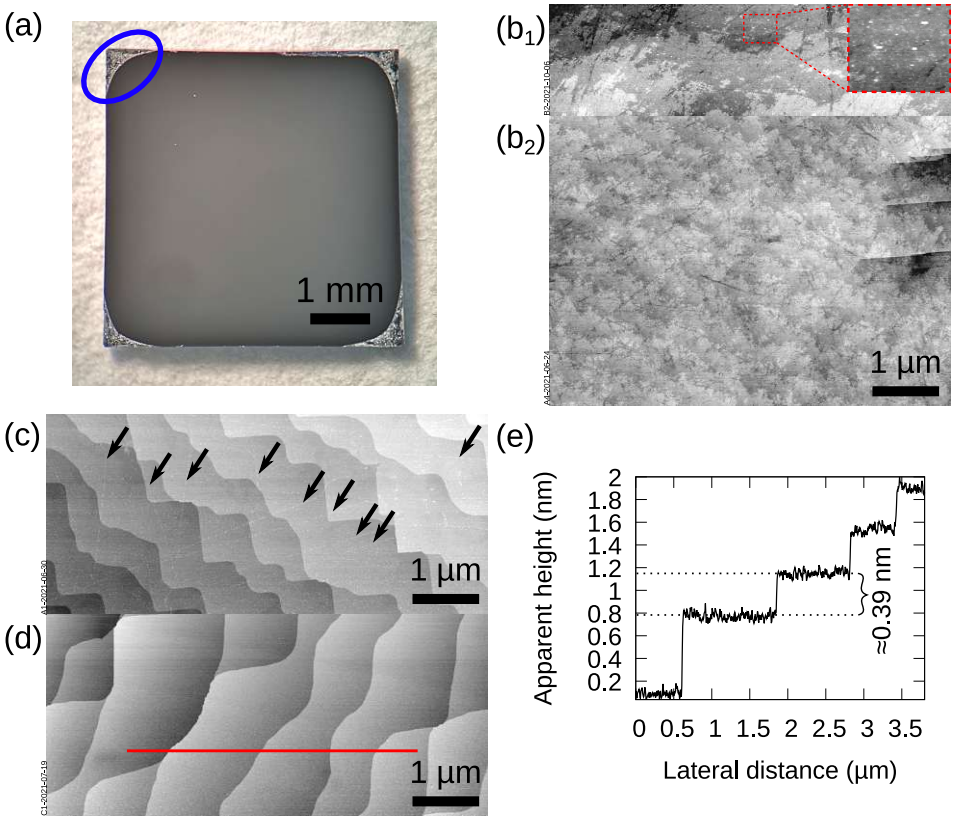

Figure 3.1: Optical microscope image, AFM images and a representative line profile $SrTiO_3(001)$. (a) The corners of the $SrTiO_3(001)$ samples are damaged if sonicated for multiple hours (marked by blue ellipse). (b_1) Typical appearance of contaminants before cleaning. The inset shows an enlarged view. (b_2) Out-of-the-box sample after cleaning. The rough steps stem from the polishing process. (c) Post-annealing with SrO segregation in form of lines (indicated by arrows). (d) Clean $SrTiO_3(001)$ exhibiting only TiO_2-terminated terraces, ready for *in-situ* handling. (e) Line profile as indicated in (d). Single and multiple (of ≈ 0.4 nm) unit-cell steps are observed.

3.1.2 *In-situ* preparation

After insertion into UHV, the substrate preparation prior to the growth followed several steps. Firstly, to test the mounting, the substrates were annealed at $T = 1000°C$ with a oxygen partial pressure of $p_{O_2} = 5 \times 10^{-6}$ mbar for 1 h. The high temperature can influence the clips elasticity, which can lead to a loose sample and therefore hinder later STM measurements. Also, substrates often crack in this phase because of thermal expansion and in case of overly-tight mounting. After this annealing step, XPS measurements show typical potential contaminants (C,

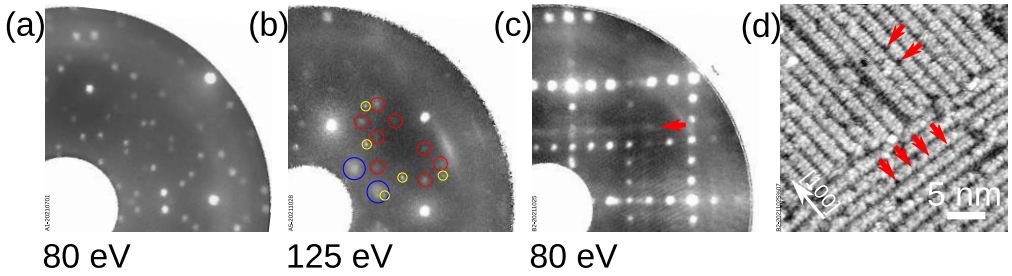

Figure 3.2: Examples for observed surface reconstructions of $SrTiO_3(001)$ before growth: (a) $(\sqrt{13} \times \sqrt{13})R33.7°$ reconstruction, (b) c(4×2) (blue circle), c(6×2) (red circle) and $(\sqrt{5} \times \sqrt{5})R26.6°$ (yellow circle). (c) (6×2) where likely periodic defects contribute to the LEED image (red arrow marks a faint line). (d) STM image of the (6 × 2) surface reconstruction measured in (c). Defects that are pointed out by red arrows appear in a periodic manner. ($U = 2.4$ V, $I = 0.12$ nA).

K, Na, Ca) from *ex-situ* treatment. These will be removed at a later stage through sputtering. After a LEED measurement ensures a relatively flat surface (by showing a reconstruction pattern), an initial STM measurement is done to verify the successful mounting. Finally, sputtering–annealing cycles and XPS measurements are continued until no more contaminants remain.

Before sputtering, the surfaces show a rich spectrum of reconstructions in LEED. Two examples before sputtering are shown in Fig. 3.2. In Fig. 3.2a, a well-ordered $(\sqrt{13} \times \sqrt{13})R33.7°$ reconstruction can be seen. In Fig. 3.2b, multiple reconstructions [c(4×2), c(6×2), $(\sqrt{5} \times \sqrt{5})R26.6°$] are visible. Although the two samples experienced similar treatments, a different reconstruction appears. One possibility could be a difference in the polishing process of the manufacturer and a resulting difference in the surface stoichiometry. $SrTiO_3(110)$ is known for changing surface reconstructions with surface composition [35].

After sputtering for 10 min at an average sputter current of $I = 2.1$ µA, followed by another round of annealing at the same conditions, the surface mostly reconstructs to a (6 × 2) surface reconstruction as observed in Ref. [36], and shown in Fig. 3.2c and Fig. 3.2d, showing representative LEED, and STM images, respectively. The additional faint lines in the LEED image (red arrow in Fig. 3.2c) likely come from regular defects visible in the STM image (red arrows in Fig. 3.2d). Their common separation is about $\Delta d = (3.1 \pm 0.3)$ nm, which

corresponds roughly to 8 times the measured lattice parameter. The measured lattice parameter is $a_{\mathrm{STO}} = (0.39 \pm 0.04)$ nm, matching the theoretical bulk lattice parameter ($a_{\mathrm{th}} = 0.39$ nm).

Because it is generally preferred to have the same surface stoichiometry on the substrate prior to the growth, i.e., the same surface reconstruction, most of the substrates used in this thesis were prepared to exhibit the (6×2) reconstruction of Fig. 3.2c. However, some substrates were also used that exhibited a mixture of the (6×2) reconstruction and one of the reconstruction seen in Fig. 3.2b.

3.2 Growth of LSMO(001)

Previous work [15] on LSMO(110) was taken into consideration for a first guess of the growth parameters for our LSMO(001) films. The laser fluence was set to 1.7 J/cm^2, substrate temperature held in the 700°C–850°C range, and O_2 background pressure in the range of $(3.5\text{–}4.1)\times10^{-2}$ mbar. The laser-pulse rate was set to 1 pulse per second.

The growth process was monitored by recording the RHEED intensity. When recording the peak intensity of the k_{00} spot in RHEED, time-resolved oscillations can be seen during growth. Fig. 3.3 shows the first four oscillations of a typical growth process for a film grown at 800°C and 4×10^{-2} mbar. The graph shows a steeply decaying trend of the overall intensity but also clear oscillations. For some growth processes, the signal-decay trend continued until noise masked the oscillation information, while for other samples the intensity–noise ratio was better. A very likely reason for this variability is the exact sample alignment which differs slightly from sample to sample. The oscillation period in Fig. 3.3 was around 64 s, which is equivalent to 64 laser pulses at 1 Hz. This oscillation period varied for different growth parameters (not shown), with higher background O_2 pressures resulting in a longer oscillation periods. This happens because of the increased scattering of ablated material for higher pressures. The oscillation period is also affected by the substrate temperature: higher temperatures induce higher evapor-

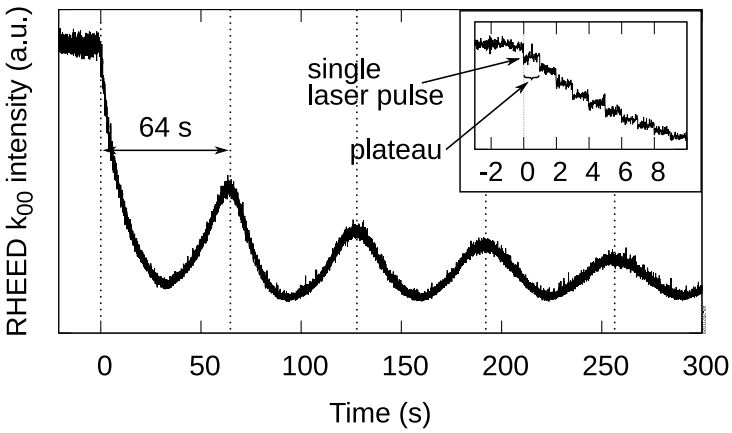

Figure 3.3: Representative RHEED intensity curve for the k_{00} spot in LSMO(001) on $SrTiO_3$(001). One oscillation (peak to peak, $\approx$ 64 s) signals the completion of a layer. A more detailed view of the first 10 s is in the upper right corner. It shows the single laser pulse events as sharp intensity drops that are followed by plateau phases in between pulses. Growth conditions: $p_{O_2} = 4 \times 10^{-2}$ mbar, $T = 800°C$.

ation from the substrate, decreasing the deposition rate (not shown).

A more detailed view of the start of the growth process is shown in Fig. 3.3, displaying a cutout of the first 10 s. Two distinct features are pointed out. Firstly, the sudden drop of intensity, which corresponds to the laser pulse and the following material transportation from the target to the sample, is shown with a black arrow. Secondly, the material diffusion phase can be identified with the plateaus, which lie in between the pulses. The growth process is stopped after 13 oscillations that can be identified with 13 layers of LSMO(001). This results in a roughly 5.1 nm thick film, where one oscillation is assumed to correspond to one full unit cell, comprising both the AO and the MnO_2 layers.

Several films were grown at slightly different parameters, resulting in different surface morphologies, often with tall clusters protruding over an otherwise flat surface (see Fig. 3.4). The formation of clusters was previously observed on LSMO(110), where it was assigned to the segregation of non-stoichiometries introduced during the growth. We speculate that a similar effect is present also on our (001)-oriented films. This is an expected result for non-ideal growth parameters. The combination of non-stoichiometric ablation from the target and preferential

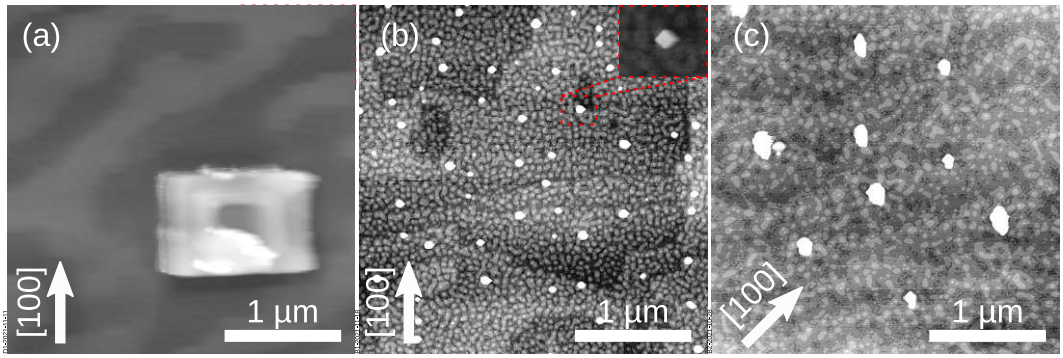

Figure 3.4: (a) AFM image of 13 layers of LSMO(001), showing a cluster ($T_a = 800°C$, $p_{O_2,a} = 4.1 \times 10^{-2}$ mbar). (b,c) AFM images of two samples with 13 layers of LSMO(001), both show clusters that range from 3–20 nm in apparent height. The inset in (b) shows details of a cluster. ($T_b = 800°C$, $p_{O_2,b} = 3.5 \times 10^{-2}$ mbar; $T_c = 850°C$, $p_{O_2,c} = 4.0 \times 10^{-2}$ mbar).

scattering in the background gas lead to this imbalance. As will be shown in Section 3.3.1, the used parameters likely lead to Mn-rich films (and therefore Mn-rich clusters). For a given fluence (here 1.7 J/cm²), heavier A-site cation concentration can be obtained by increasing the oxygen pressure. The idea is that this leads to increased scattering of the lighter B-site species. Finally, it can be argued that the optimal parameters for LSMO(110) do not exactly apply for LSMO(001), possibly because of differences in the surface reconstructions or different sticking probabilities.

The choice of a thickness of 13 layers is motivated by multiple reasons. Firstly, the non-stoichiometries introduced when the parameters are not ideal accumulate as the thickness increases, producing rough surfaces that are difficult to work with. It is known from experiments on LSMO(110) that these films can incorporate non-stoichiometries by a changed surface reconstruction before forming LaO_x or MnO_x clusters [15]. Secondly, for LSMO(001), insulating effects have been reported for thin films around and below 10 unit cells [6]. Finally, RHEED measurement oscillations were nicely visible only until around 13 layers, where their disappearance points to island growth.

Figure 3.4 shows multiple samples with unsuccessful growths, in the sense that flat morphologies were not achieved and non-stoichiometries emerged in the form

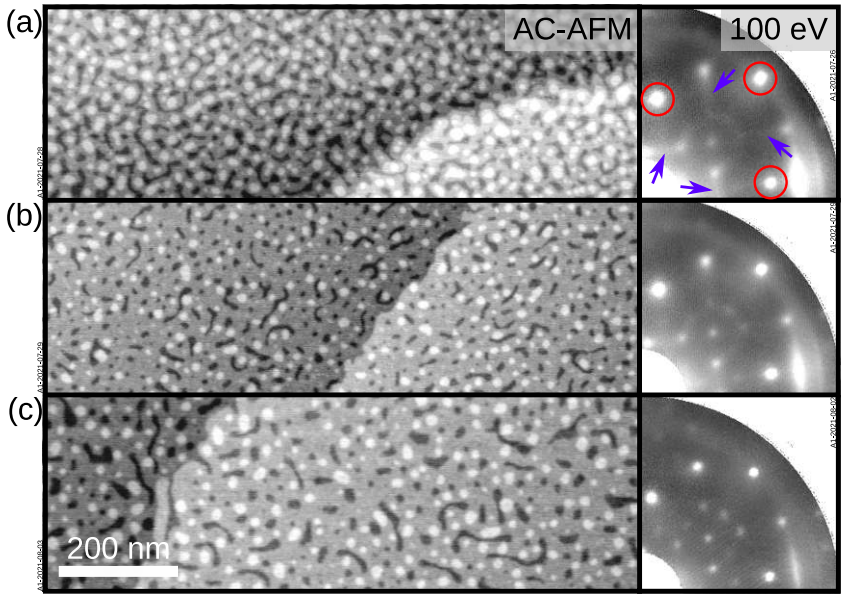

Figure 3.5: AFM images of a LSMO(001) film of 13 layer thickness and the corresponding LEED images. The sample was removed from UHV for the AFM measurement after each step and annealed as described upon reinsertion. (a) After growth at 700°C in oxygen partial pressure of 4.1×10^{-2} mbar, there are 3–4 layers exposed. The LEED pattern shows streaks (blue arrows) in between the main (0,1), (1,0) and (1,1) spots (red circles); (b,c) Post-annealing at higher temperatures in oxygen (T_b = 750°C, T_c = 800°C, p_{O_2} = 4.1×10^{-2} mbar) facilitates the flattening of the film and decreases the number of islands. The LEED reconstruction-spots become increasingly sharp with every iteration.

of clusters. The sample shown in the AFM image in Fig. 3.4a was grown at T_a = 800°C, $p_{O_2,a} = 4.1 \times 10^{-2}$ mbar, and could not be measured in STM due to loose mounting. Hence, it was removed from UHV and measured in AFM in air. The appearance resembles lanthanum-oxide-rich clusters in LSMO(110) systems that were identified from XPS analysis [15]. It should be noted that this was the only sample with this kind of clusters appearing. The LSMO(001) films in Fig. 3.4b,c were grown at slightly different conditions (T_b = 800°C, $p_{O_2,b} = 3.5 \times 10^{-2}$ mbar; T_c = 850°C, $p_{O_2,c} = 4.0 \times 10^{-2}$ mbar). Both show clusters that differ in size and number. Often the apparent height of the clusters (3–20 nm) is greater than the thickness of the LSMO(001) film itself (5.5 nm). The inset in Fig. 3.4b shows the square appearance of a cluster with better contrast.

The thin film stoichiometry depends very sensitively on the growth parameters

and can therefore be hard to control. Optimized growth conditions are yet to be determined for this system, but one successful growth is shown in Fig. 3.5a. This LSMO film was grown at 700°C in a O_2 pressure of 4.1×10^{-2} mbar, followed by 30 minutes of holding the sample at 700°C. The surface shows 3–4 exposed layers of LSMO, the main features being rough circular islands on top of a partly grown layer, and underneath a third fully grown layer. The corresponding LEED image on the right side of the Figure shows clearly a surface reconstruction. This can be deduced by identifying the intense (0,1), (1,0) and (1,1) spots (red circles) and the dimmer streaks (blue arrows) and diffraction spots in between. Two additional annealing steps at 750°C and 800°C at the same O_2 background pressure are shown in Fig. 3.5b,c. In between annealing steps, the sample was removed from UHV for the AFM measurement. To regain a contamination-free surface the annealing steps were sufficient, while also facilitating surface flattening. A clear progress is visible in the size of the features as well as the sharpness of the LEED pattern. In Fig. 3.5c, very sharp spots can be seen which will be analysed further in Section 3.3. It should be noted that for the 13-layers-thick films we measured, this was the only LEED pattern we observed for growth temperatures ranging from 700°C to 850° and O_2 background pressures in the $(3.5–4.1) \times 10^{-2}$ mbar range (with minimal deviations shown further below in Section 3.3.1).

The decrease of the roughness of the surface with each annealing step is likely a result of the increased surface diffusion caused by the elevated temperature. It was previously shown that a variation of growth temperature and O_2 background pressure, which can be related to the oxygen chemical potential μ_{O_2} (see Eq. 2.1), can have a great impact on a surface's flatness [18].

Our LEED findings can be compared to the study by Kelley et al. [13] in the literature. The authors have deposited LSMO(001) on $NdGaO_3$(001) pseudocubic substrates, which also has only a small lattice mismatch of -0.52% with slight compressive stress compared to the tensile strain of 0.74% with $SrTiO_3$(001). They grew 15 unit cell thick films from a $La_{0.7}S_{0.3}MnO_3$ target at 700°C and in $p_{O_2} =$ 1.3 mbar. After depositing at a laser pulse rate of 10 Hz the substrates were

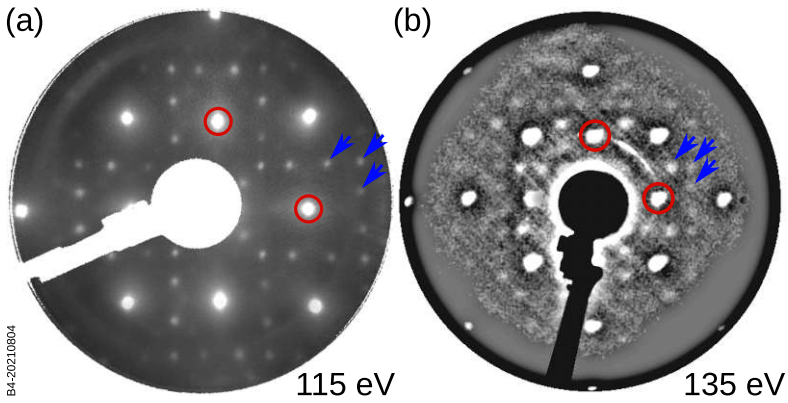

Figure 3.6: Comparison between LEED images of LSMO(001) films taken at the Technical University of Vienna and by Kelley et al. [13] at the Oak Ridge National Laboratory. (a) 115 eV LEED image of a $La_{0.8}S_{0.2}MnO_3$ film of 13 unit cells grown on $SrTiO_3$(001) at $T = 800°C$, $p = 4.0 \times 10^{-2}$ mbar. The main diffraction spots are marked with red circles. (b) 135 eV LEED image, of a $La_{0.7}S_{0.3}MnO_3$ film of 15 unit cells grown on $NdGaO_3$(001) at $T = 700°C$, $p = 0.13$ mbar. The red circles in both images are equivalent. With enhanced contrast on (b), it can be seen that the two structures are equivalent or at least very similar. Blue arrows point out similarities. Panel (b) is adapted with permission from [13]. Copyright 2021 American Chemical Society.

annealed for 4 h at the same pressure. The laser fluence was 1.2 J/cm^2 during growth and preablation.

These PLD parameters are not necessarily relevant, as reproducing growth from these can be very challenging from chamber to chamber [37]. Therefore, it might be impossible to draw conclusions from the comparison of growth parameters without further tests. What likely can be compared are the nominal composition of their target and the different substrate. Despite these differences, their LEED data looks very similar to ours. This points to a robust and adaptable structure.

Figure 3.6a,b shows a direct comparison between our LEED data and of Ref. [13] taken at similar energies. The LEED image in Fig. 3.6b was accentuated in contrast. Equivalent (1,0) and (0,1) diffraction spots are marked by red circles. The LEED pattern in (b) is best visible around the right red circle. It shows the same periodicities as in (a) with a few examples pointed out by blue arrows. Noticeably, the diffraction spots in Fig. 3.6b are rather diffuse in comparison. This could stem from a suboptimal configuration of their LEED system or from imperfect ordering of the surface reconstruction.

In Ref. [13], the authors assigned the observed reconstruction to a model for a long-range (6×6) unit cell, backed by LEED-IV calculations with a reliability factor R [38] around 0.9—which already refutes their structural model. The reliability factor $R \geq 0$ reveals the statistical correlation between model and experimental data with higher values implying no statistical correlation.

3.3 Characterization of flat LSMO films

In this section, comparison of data of different techniques and subsequent analysis of selected STM images will lead to a model for the reconstruction exposed by our LSMO(001) films. The terminating layer shows a complicated 4-fold symmetric reconstruction. This surface has characteristics akin to quasi-crystals and can be approximated with an (10×10) unit cell. While not matching the experimental data exactly, the suggestions should give insights into the surface periodicity and guide future studies to precisely establish the surface atomic structure and composition.

3.3.1 Effect of sputtering on the surface structure and composition

In order to grow thick stoichiometric films, it is often useful to analyse the surface composition of thin films and how this changes upon sputtering–annealing cycles. Figure 3.7a shows an STM image of the as-grown 5.1 nm-thick film ($T = 800$°C, $p_{O_2} = 4.0 \times 10^{-2}$ mbar). A line profile indicated in blue is shown in the graph in Fig. 3.7c as the grey profile line. The step size is approximately 0.4 nm, which is close to the expected step size for a single LSMO unit cell in [001] direction. In Fig. 3.7b, the surface is shown after two sputter–anneal cycles. The surface was sputtered for 70 s and 90 s in the two cycles respectively and each time annealed at growth conditions for 1 h. A new phase appears, which can be seen from the corresponding line profile (at half the unit cell). The new phase is preferentially

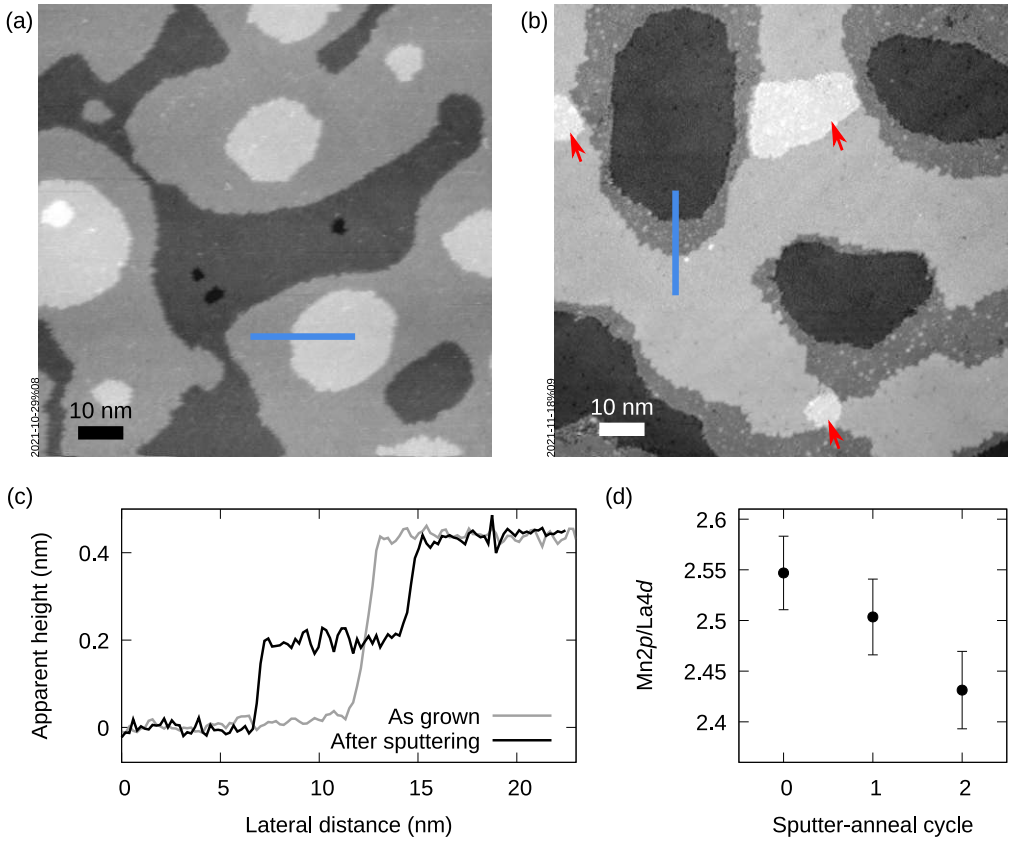

Figure 3.7: (a,b) STM images of an as-grown film ($T = 800°C$ and $p_{O_2} = 4.0 \times 10^{-2}$ mbar) and after two rounds of sputtering (70 s and 90 s) and annealing at the growth conditions for 1 h. The blue lines represent line profiles and red arrows point to islands a newly appearing phase [(a) $U_s = 2.0$ V, $I_t = 0.09$ nA, (b) $U_s = 5.2$ V, $I_t = 0.17$ nA]. (c) Apparent height profiles of step edges in the images. After sputtering, 'half-steps' appear. (d) Integrated area ratio of Mn $2p$ over La $4d$ peaks as measured in XPS, evaluated with a Shirley-type background subtracted. Data-points at zero and two sputter–anneal cycles correspond to images (a) and (b).

located at step edges. Islands (indicated by red arrows) are never isolated and do not form holes in the middle of a terrace. Furthermore, bright features can be seen on the new areas, suggesting a more defected, or more reactive surface.

Finally, the effect of the sputter–anneal procedure can also be seen in the ratio of the integrated areas of Mn $2p$ and La $4d$ in Fig. 3.7d. The decrease of the preferentially sputtered Mn in combination with the newly appearing phase at the 'half-steps' leads to the conclusion that the surface is initially Mn rich. The other appearing phase can then be identified as A-site rich.

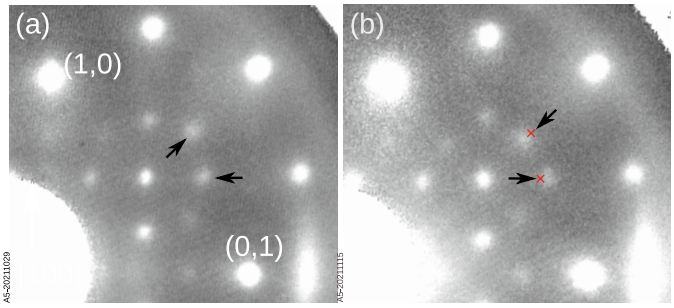

Figure 3.8: Two LEED images at 100 eV of LSMO(001) (13 unit cells thin) films. (a) is the reconstruction as grown and (b) is a slightly changed pattern after short sputtering. Arrows and the red crosses in (b) indicate the small differences between them.

Figure 3.8 highlights the effect of sputtering and annealing on the surface reconstructions of LSMO(001), as seen from LEED. Figure 3.8a shows the surface reconstruction of a film as grown at $T = 800°C$ and $p_{O_2} = 4.0 \times 10^{-2}$ mbar. Figure 3.8b shows the same film after a short (70 s) sputtering followed by annealing for 1 h at growth conditions. The LEED images vary slightly as shown by the arrows, which point in the direction of relative change between the images. In Fig. 3.8b, the red markers show the positions of the spots before sputtering (Fig. 3.8a). The results point to small changes in the reconstruction driven by small changes in the surface stoichiometry by preferential sputtering or by partial reevaporation of Mn atoms during annealing.

Surface reconstructions of LSMO(110) has been shown to be very sensitive to the surface stoichiometry [2]. Also, bulk manganese oxides (MnO_x, $1 \leq x \leq 2$) are known to crystallize in more than 30 different naturally occuring crystal forms of oxides/hydroxides [39]. Although 2D and 3D systems are not to be mixed up, it seems reasonable that the inherent complexity of bulk MnO_x can lead also to increased variations in MnO_x terminated thin films. For example, in two-dimensional manganese oxide nanolayers on Pd(100), a wealth of complicated superstructures depending on the oxidation state have been reported [40].

3.3.2 Identification of a surface reconstruction with quasi-crystalline character

Figure 3.9 compares the fast-fourier transforms (FFT) extracted from representative STM images with the corresponding LEED data. The two STM images were taken on the same sample at similar conditions. In between, the tip termination changed multiple times, and the tunnelling voltage was slightly decreased from 4.0 V to 3.1 V, which led to a difference in the FFT. The white circles in Fig.3.9a,c mark the (0,1) spot at a periodicity of (0.40 ± 0.04) nm. This corresponds to the bulk unit cell of LSMO with a lattice parameter of $a = 0.39$ nm. The other contributions to the reconstruction pattern are highlighted with the same colors in the FFT and in the LEED image. The observed periodicities come from the whole surface without any localized preference. This can be deduced from analysis of the inverse FFT (not shown), where isolating single periodicities in the FFT leads to filtered real-space images (inverse FFT) that show the periodicity-origin areas. For a complicated reconstruction like this, one would expect either multiple domains or a very large unit cell. Neither can be seen in the images.

The two phases that were mentioned earlier in the section, namely Mn-rich and La-rich, can be identified in the atomically resolved STM image in Fig. 3.9a. When isolated, the leftmost terrace, identified with the Mn-rich phase, contributes in the FFT to the oblique reconstruction also seen in the LEED in Fig. 3.9c. When isolating the 'half-step' terrace, identified with the La-rich phase, only contributions to the primary (1×1) spots persist (e.g. white circle in Fig. 3.9c)

Preliminary analysis of the surface

Here a surface characterization of LSMO(001) films with a thickness of 13 unit cells (around 5.1 nm) is shown. Figure 3.10a shows an atomically resolved STM image of the reconstructions identified above. The arrangement of the bright features is looked at carefully. In order to reduce noise and to isolate the structure, a feature finder was used. This places single points at the center of similar features

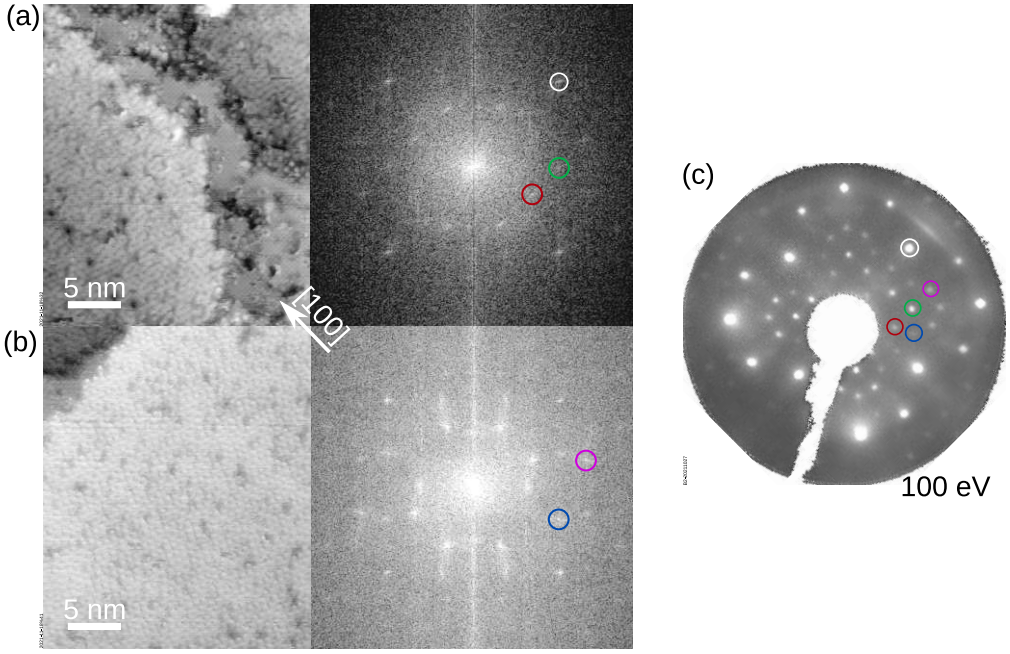

Figure 3.9: (a,b) Two STM images of the same sample, measured in the same session [(a) $U_s = 4.0$ V, $I_t = 0.12$ nA, (b) $U_s = 3.1$ V, $I_t = 0.13$ nA]. In (a) three terraces can be seen, where the film shows two different structures. Two of the three terraces show the oblique reconstruction and the one in the middle has a 1×1 periodicity and is separated by half a unit-cell step from the neighbouring ones. Different voltages and a STM tip that likely changed, cause features to be imaged slightly differently. Combining the FFT images of multiple tip configurations, one can compare the periodicities to the representative LEED image in (c).

based on a manually selected example with adjustable tolerances. This is shown in Fig. 3.10b, where an enlarged section of the point mask demonstrates the isolated periodicity of the bright features. The FFT of this point mask is almost identical to the one shown in Fig. 3.9b, but has better contrast because of the reduced noise (not shown).

To gain insights into the periodicity, a point auto-correlation image (Fig. 3.10c) is constructed from the mask. This simply visualizes, starting from any feature point in the mask, the probability to find another point in any direction. Starting from the center, the most probable spots for another feature lie on the (1×1) grid, at preferred distances of $\sqrt{5} \times a_{(1\times1)}$. For a regularly spaced lattice (or well ordered superstructure), one would expect long-range order. In the point auto-correlation this would be visible by similar probabilities at equidistant positions in certain

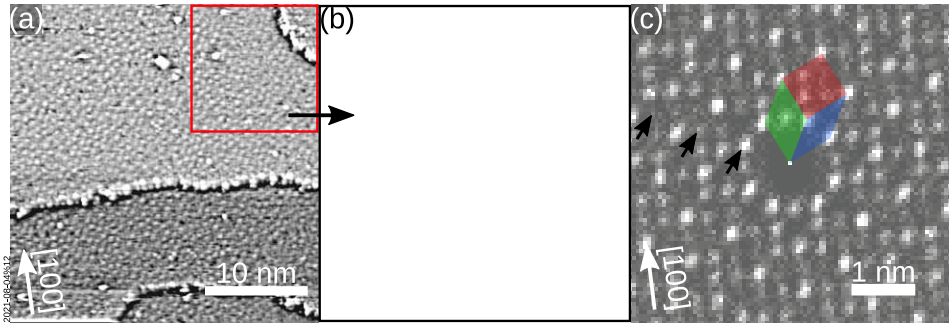

Figure 3.10: (a) STM image of the LSMO(001) film. Bright features are distributed in a complicated way. (b) A small part of the feature point-mask is shown. (c) From the feature point-mask, a point-autocorrelation is constructed. The probability to encounter another point in the mask is illustrated by intensity. To try to understand this short range order, three tiles are placed with corners at high-intensity spots.

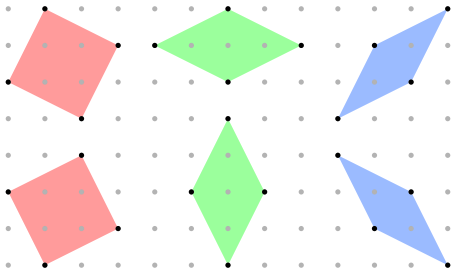

Figure 3.11: The three tiles from Fig. 3.10c can only be placed in certain ways on the underlying (grey) 1×1 grid of the LSMO(001) plane. For each tile, the two possibilities are shown.

directions (as indicated by the black arrows in Fig. 3.10c). The presented data does not show this behaviour, while still exhibiting short-range order. Inspired by the most common short-range periodicities visible in Fig. 3.10c, three different tiles are found.

The tiles that supposedly make up the structure are shown in detail in Fig. 3.11. The grey coloured points signify the underlying (1×1) lattice of the (001) surface. The features/points in Fig. 3.10 mark the corners of the tiles (black dots). These three building blocks can only be arranged in this way on the square lattice. Since our building blocks have to fit on top of the grid, the angles can be shown to be 90° (square), $\approx 53.1°$ (acute-angle green rhombus) and $\approx 38.9°$ (acute-angle blue rhombus). Patterns made from these blocks share some similarities with the so-called Ammann–Beenker tiling, where there is only a square and a 45° rhombus

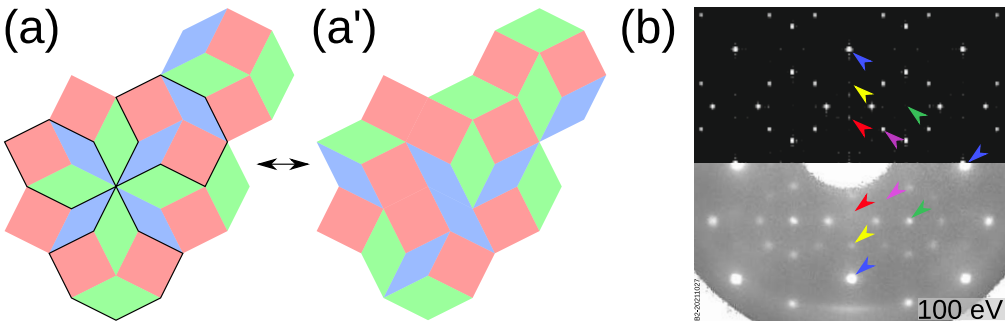

Figure 3.12: (a,a') Examples for 10×10 unit cells are shown. In (a), three common tile combination motifs are indicated by a black border. In (a'), one of many possible variations of this cell is demonstrated. (b) The FFT of (a) is compared with a LEED image. The FFT image was produced in ImageJ [23] after placing a point-like feature at each corner of the tiles. While many diffraction spots (marked by coloured arrows) fit the measurement well, some intensities do not match (i.e. yellow, purple, green).

(see, e.g., Ref. [41] Fig. 1b).

From these blocks, aperiodic tilings can be made. Figure 3.12a shows an (10×10)-unit-cell example. Smaller tile motifs are shown with a black border. A classification of this tiling and its variants goes beyond the scope of this thesis. There are, however, many works on tilings and as a reference the 'tilings encyclopedia' is given [42]. Just to demonstrate another possibility, a variation is included in Fig. 3.12a', which covers the same (10×10)-unit-cell area with tiles placed differently in the interior. This highlights why it is not straightforward to find unit cells in the STM data.

In Fig. 3.12b, the FFT of the pattern shown in Fig. 3.12a is compared directly to the LEED of the LSMO(001) surface. The blue arrows mark the main diffraction spots that also match with the (1×1) periodicities of the square lattice substrate. A few differences are pointed out be the yellow, purple and green arrows.

For a reconstruction that only shows spots marked by blue and green arrows, one would describe it as a $(\sqrt{2} \times \sqrt{2})R45°$ reconstruction. The '$\sqrt{2}$-spot' (green) is only sometimes faintly visible in the FFT of STM (see, e.g., Fig. 3.9a). The rhombohedral nature of bulk $La_{0.8}S_{0.2}MnO_3$ might play a role here. It has been shown using high-angle annular dark field scanning transmission electron microscopy (HAADF-STEM) that LSMO on $SrTiO_3$(001) will relax into its rhombo-

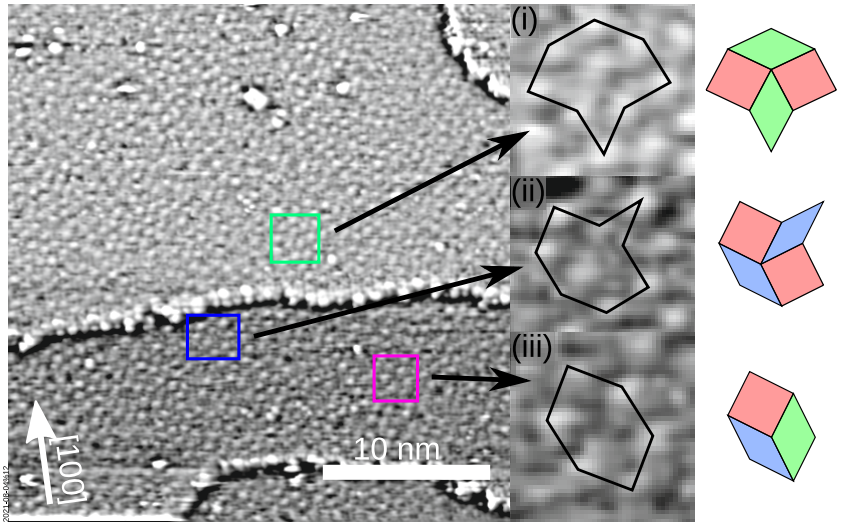

Figure 3.13: Examples for the tile-motifs introduced in Fig. 3.12a. (i–iii) Magnified areas. Black lines are drawn to guide the eye. The tiles are often not exact. As it can be seen in (iii), features are sometimes distorted compared to the tiles.

hedral bulk structure very close to the interface [10]. Therefore it may be argued, that the LEED measurement picks up the rhombohedral $(\sqrt{2} \times \sqrt{2})R45°$ unit cell (caused by tilted MnO_6 octahedra) from below the surface.

Finally, coming back to the STM data in Fig. 3.13, three examples for small tile combinations are pointed out. The examples in Fig. 3.13i,ii match the proposed structures quite well, when fitted to the bright features. Figure 3.13iii, on the other hand, also shares the characteristic outline, but the central (inner) feature does not fit well on the proposed structure. Regular reoccurrences of these motifs or other unit cells, similar to the examples shown in Fig. 3.12a or Fig. 3.13, can not be identified, which points to the quasi-crystal like properties of this surface reconstruction.

3.4 Conclusions

This thesis was focused on the PLD growth and surface characterization of LSMO(001) films grown on Nb-doped $SrTiO_3$(001) single crystals prepared in UHV. The goal was to produce single-crystalline films useable as a model of (001)-oriented bulk LSMO and to investigate the surface structures. The presented data on the preparation of 13 unit cells thick LSMO(001) films is a stepping stone in achieving this.

The $SrTiO_3$ substrates were carefully cleaned and annealed *ex-situ*, and further cleaned and characterized in UHV. $SrTiO_3$(001) can show a wide spread of surface reconstructions, which appear not to have a primary impact on film growth.

Similarly to previous studies, the films' morphology and composition was significantly affected by the PLD parameters. A few sucessful growths were carried out with a thickness of 13 unit cells. These films show a complex surface reconstruction with a 2D quasicrystal character. More data and density functional theory calculations will be needed for a conclusive model. Quasicrystals have been measured before in solids and surfaces. Natural ones found primarily in meteorites [43]. In surfaces, perovskite oxide single-layer-thick films have been previously reported for 2D oxide quasicrystal structures [44].

In the light of recent research, it is anticipated that future studies on LSMO(001) will reveal a broad spectrum of surface reconstructions—similar to the results of LSMO(110) and other perovskite oxides [15].

Acknowledgement

The warm welcome I received in the Surface Physics Group at the Vienna University of Technology made it feel like a second home to me, in a time of social stagnation and quarantined emotions. Many thanks to Prof. Ulrike Diebold for her excellent supervision, who provided me shelter in her group and the opportunity to see the world of academia. I would like to recognize the invaluable guidance and assistance of Dr. Michele Riva and Erik Rheinfrank for their continued support in the laboratory and the many discussions about the incredibly complicated data we measured. I would also like to thank Dr. Giada Franceschi, who gave not only great linguistic advice, but also helpful input for the experiments. I am also very grateful for my friends and family, for always having my back over the past years. Finally, an unreserved apology goes to those near me that had to endure my frustration at times, even though I hope that the good times made up for it.

Financial Support from the Austrian Science Fund FWF, Project F81 SFB TACO, is gratefully acknowledged.

Bibliography

[1] G. Franceschi et al. 'Growth of $In_2O_3(111)$ thin films with optimized surfaces'. In: *Physical Review Materials* 3.10 (2019), p. 103403. DOI: 10.1103/physrevmaterials.3.103403.

[2] G. Franceschi et al. 'Two-dimensional surface phase diagram of a multicomponent perovskite oxide: $La_{0.8}Sr_{0.2}MnO_3(110)$'. In: *Physical Review Materials* 5.9 (2021), p. l092401. DOI: 10.1103/physrevmaterials.5.l092401.

[3] M. Riva et al. 'Pushing the detection of cation nonstoichiometry to the limit'. In: *Physical Review Materials* 3.4 (2019), p. 043802. DOI: 10.1103/physrevmaterials.3.043802.

[4] T. K. Andersen, D. D. Fong and L. D. Marks. 'Pauling's rules for oxide surfaces'. In: *Surface Science Reports* 73.5 (2018), pp. 213–232. DOI: 10.1016/j.surfrep.2018.08.001.

[5] J. Hemberger et al. 'Structural, magnetic, and electrical properties of single-crystalline $La_{1-x}Sr_xMnO_3$ ($0.4 < x < 0.85$)'. In: *Physical Review B* 66.9 (2002), p. 094410. DOI: 10.1103/physrevb.66.094410.

[6] M. Huijben et al. 'Critical thickness and orbital ordering in ultrathin $La_{0.7}Sr_{0.3}MnO_3$ films'. In: *Physical Review B* 78.9 (2008), p. 094413. DOI: 10.1103/physrevb.78.094413.

[7] B. Kim et al. 'Finite size effect and phase diagram of ultra-thin $La_{0.7}Sr_{0.3}MnO_3$'. In: *Solid State Communications* 150.13-14 (2010), pp. 598–601. DOI: 10.1016/j.ssc.2009.12.041.

[8] Z. Liao and J. Zhang. 'Metal-to-Insulator Transition in Ultrathin Manganite Heterostructures'. In: *Applied Sciences* 9.1 (2019), p. 144. DOI: 10.3390/app9010144.

[9] F. Lan et al. 'Observing a previously hidden structural-phase transition onset through heteroepitaxial cap response'. In: *Proceedings of the National Academy of Sciences* 116.10 (2019), pp. 4141–4146. DOI: 10.1073/pnas.1819641116.

[10] L. Chen et al. 'Surface and interface properties of $La_{2/3}Sr_{1/3}MnO_3$ thin films on $SrTiO_3$ (001)'. In: *Physical Review Materials* 3.4 (2019), p. 044407. DOI: 10.1103/physrevmaterials.3.044407.

[11] H. Chen et al. 'Thickness-driven first-order phase transitions in manganite ultrathin films'. In: *Physical Review B* 99.21 (2019), p. 214419. DOI: 10.1103/physrevb.99.214419.

[12] H. Chen et al. 'Antiferromagnetic metallic state and low-temperature magnetoresistance in epitaxial $La_{0.85}Sr_{0.15}MnO_3$ films'. In: *Applied Surface Science* 569 (2021), p. 151032. DOI: 10.1016/j.apsusc.2021.151032.

[13] K. P. Kelley et al. 'Exotic Long-Range Surface Reconstruction on $La_{0.7}Sr_{0.3}MnO_3$ Thin Films'. In: *ACS Applied Materials & Interfaces* 13.7 (2021), pp. 9166–9173. DOI: 10.1021/acsami.0c20166.

[14] G. Franceschi et al. 'Atomically resolved surface phases of $La_{0.8}Sr_{0.2}MnO_3$(110) thin films'. In: *Journal of Materials Chemistry A* 8.43 (2020), pp. 22947–22961. DOI: 10.1039/d0ta07032g.

[15] G. Franceschi. *Pulsed laser deposition of functional oxides with atomic scale control*. PhD Thesis, 2020.

[16] G. Rijnders and D. H. A. Blank. 'Growth Kinetics During Pulsed Laser Deposition'. In: *Pulsed Laser Deposition of Thin Films*. John Wiley & Sons, Inc., 2006, pp. 177–190. DOI: 10.1002/9780470052129.ch8.

[17] K. Oura. *Surface Science An Introduction. An Introduction*. Springer Berlin Heidelberg, 2003, p. 440. ISBN: 9783642056062.

[18] G. Franceschi et al. 'Reconstruction changes drive surface diffusion and determine the flatness of oxide surfaces'. In: *Journal of Vacuum Science & Technology A* 40.2 (2022), p. 023206. DOI: 10.1116/6.0001704.

[19] B. Voigtländer. *Scanning Probe Microscopy*. Springer Berlin Heidelberg, 2015. DOI: 10.1007/978-3-662-45240-0.

[20] H. Uchida et al. 'Single-atom manipulation on the Si(111)7 × 7 surface by the scanning tunneling microscope (STM)'. In: *Surface Science* 287-288 (1993), pp. 1056–1061. DOI: 10.1016/0039-6028(93)91126-a.

[21] D.P. Woodruff. 'Low Energy Electron Diffraction'. In: *Reference Module in Materials Science and Materials Engineering*. Elsevier, 2016. DOI: 10.1016/b978-0-12-803581-8.03400-7.

[22] K. K. Kolasinski. *Surface Science*. Wiley John + Sons, 2012. 574 pp. ISBN: 1119990351. URL: https://www.ebook.de/de/product/18118424/kurt_k_kolasinski_surface_science.html.

[23] C. A. Schneider, W. S. Rasband and K. W. Eliceiri. 'NIH Image to ImageJ: 25 years of image analysis'. In: *Nature Methods* 9.7 (2012), pp. 671–675. DOI: 10.1038/nmeth.2089.

[24] H. Lüth. 'Scattering from Surfaces and Thin Films'. In: *Graduate Texts in Physics*. Springer International Publishing, 2015, pp. 129–216. DOI: 10.1007/978-3-319-10756-1_4.

[25] M. P. Seah and W. A. Dench. 'Quantitative electron spectroscopy of surfaces: A standard data base for electron inelastic mean free paths in solids'. In: *Surface and Interface Analysis* 1.1 (1979), pp. 2–11. DOI: 10.1002/sia.740010103.

[26] K. Siegbahn. *ESCA: Atomic, Molecular and Solid State Structure Studied by Means of Electron Spectroscopy*. Kunglia Vetenskap-Societeten Uppsala: Nova acta Regiae Societate's Uppsaliensis: Serie 4. Almqvist & Wiksells, 1967. URL: https://books.google.ch/books?id=5O1sugEACAAJ.

[27] S. Doniach and M. Sunjic. 'Many-electron singularity in X-ray photoemission and X-ray line spectra from metals'. In: *Journal of Physics C: Solid State Physics* 3.2 (1970), pp. 285–291. DOI: 10.1088/0022-3719/3/2/010.

[28] J. Osterwalder. *Electron Based Methods: 3.2.2 Photoelectron Spectroscopy and Diffraction*. 2013. DOI: 10.1002/9783527680535.ch5.

[29] G. Binnig, C. F. Quate and Ch. Gerber. 'Atomic Force Microscope'. In: *Physical Review Letters* 56.9 (1986), pp. 930–933. DOI: 10.1103/physrevlett.56.930.

[30] *Atomic force microscope block diagram: Accessed April 2022*. URL: https://commons.wikimedia.org/wiki/File:Atomic_force_microscope_block_diagram.svg.

[31] J. G. Connell et al. 'Preparation of atomically flat $SrTiO_3$ surfaces using a deionized-water leaching and thermal annealing procedure'. In: *Applied Physics Letters* 101.25 (2012), p. 251607. DOI: 10.1063/1.4773052.

[32] G. Koster et al. 'Quasi-ideal strontium titanate crystal surfaces through formation of strontium hydroxide'. In: *Applied Physics Letters* 73.20 (1998), pp. 2920–2922. DOI: 10.1063/1.122630.

[33] J. E. Boschker and T. Tybell. 'Qualitative determination of surface roughness by in situ reflection high energy electron diffraction'. In: *Applied Physics Letters* 100.15 (2012), p. 151604. DOI: 10.1063/1.3701610.

[34] S.A. Chambers et al. 'Unintentional F doping of $SrTiO_3$(001) etched in HF acid-structure and electronic properties'. In: *Surface Science* 606.3-4 (2012), pp. 554–558. DOI: 10.1016/j.susc.2011.11.029.

[35] M. Riva et al. 'Epitaxial growth of complex oxide films: Role of surface reconstructions'. In: *Physical Review Research* 1.3 (2019), p. 033059. DOI: 10.1103/physrevresearch.1.033059.

[36] M. R. Castell. 'Nanostructures on the $SrTiO_3$(001) surface studied by STM'. In: *Surface Science* 516.1-2 (2002), pp. 33–42. DOI: 10.1016/s0039-6028(02)02053-8.

[37] A. Ojeda-G-P, M. Döbeli and T. Lippert. 'Influence of Plume Properties on Thin Film Composition in Pulsed Laser Deposition'. In: *Advanced Materials Interfaces* 5.18 (2018), p. 1701062. DOI: 10.1002/admi.201701062.

[38] J. B. Pendry. 'Reliability factors for LEED calculations'. In: *Journal of Physics C: Solid State Physics* 13.5 (1980), pp. 937–944. DOI: 10.1088/0022-3719/13/5/024.

[39] S. K. Ghosh and H. Rahaman. 'Noble Metal–Manganese Oxide Hybrid Nanocatalysts'. In: *Noble Metal-Metal Oxide Hybrid Nanoparticles*. Elsevier, 2019, pp. 313–340. DOI: 10.1016/b978-0-12-814134-2.00009-7.

[40] F. Li et al. 'Two-dimensional manganese oxide nanolayers on Pd(100): the surface phase diagram'. In: *Journal of Physics: Condensed Matter* 21.13 (2009), p. 134008. DOI: 10.1088/0953-8984/21/13/134008.

[41] J. E. S. Socolar. 'Simple octagonal and dodecagonal quasicrystals'. In: *Physical Review B* 39.15 (1989), pp. 10519–10551. DOI: 10.1103/physrevb.39.10519.

[42] D. Frettlöh, E. Harriss and F. Gähler. *Tilings encyclopedia: accessed March 2022*. URL: https://tilings.math.uni-bielefeld.de/.

[43] L. Bindi et al. 'Collisions in outer space produced an icosahedral phase in the Khatyrka meteorite never observed previously in the laboratory'. In: *Scientific Reports* 6.1 (2016). DOI: 10.1038/srep38117.

[44] S. Förster et al. 'Quasicrystals and their Approximants in 2D Ternary Oxides'. In: *physica status solidi (b)* 257.7 (2019), p. 1900624. DOI: 10.1002/pssb.201900624.